Weierstraß–Institut
für Angewandte Analysis und Stochastik

im Forschungsverbund Berlin e.V.

Preprint ISSN 0946 – 8633

Flow and thermal convection in full-zone liquid bridges of wide-ranging aspect ratio

Dominic Davis [1], Frank Smith [2]

submitted: 5th March 2002

[1] Weierstrass Institute for Applied Analysis and Stochastics, Mohrenstraße 39, D - 10117 Berlin, Germany
E-Mail: davis@wias-berlin.de

[2] Department of Mathematics, University College London, Gower Street, London WC1E 6BT, UK
E-mail: frank@math.ucl.ac.uk

Preprint No. 720
Berlin 2002

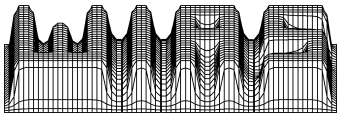

2000 *Mathematics Subject Classification.* 35Q30, 35B40, 65M60, 65N06, 75D45.

Key words and phrases. liquid bridges, crystal growth, floating-zone, axisymmetric, Navier–Stokes equations, thermocapillarity, buoyancy, asymptotic, finite-element.

Edited by
Weierstraß–Institut für Angewandte Analysis und Stochastik (WIAS)
Mohrenstraße 39
D — 10117 Berlin
Germany

Fax: + 49 30 2044975
E-Mail (X.400): c=de;a=d400-gw;p=WIAS-BERLIN;s=preprint
E-Mail (Internet): preprint@wias-berlin.de
World Wide Web: http://www.wias-berlin.de/

Abstract

Flow and thermal effects concerned with liquid crystal growth are studied nonlinearly for low Prandtl numbers, in an axisymmetric steady configuration with endwalls present. Full solutions are obtained by finite element simulation to examine the influences of aspect ratio, Marangoni number and Rayleigh number. In particular a 'lemonhead' phenomenon is found in which the velocity profiles acquire a very localised bell-shaped form as jet like flow starts to emerge, when the relative size of the Marangoni number increases above a finite critical value which is identified. Wide-domain and narrow-domain analyses are then presented, showing favourable agreement with the full solutions and explaining the impact of the end walls on the motion, especially through slender flow modelling in the narrow-domain context. Sensitive scalings for the relative effects of the Marangoni and Rayleigh numbers emerge, and the lemonhead phenomenon is also accounted for as a substantial change in the convective flow structure.

1 Introduction

Semiconductor crystals and their properties are of central importance in the fields of computer technology and communications. Virtually all modern electronic devices are built from single crystals, which are normally processed using one of two methods: the Czochralski method or the floating-zone (FZ) method. In both cases, raw polycrystalline material is melted and either placed in a crucible (as with the former) or else suspended between coaxial discs to form a liquid bridge (as with the latter). Then, under the influences of heat and mass transfer, the impurities within the melt are eliminated. Although an important method especially for the growth of large crystals in terrestrial settings, a well-established problem with the Czochralski method is that further impurities are often introduced from the contact of the melt with the crucible walls. On the other hand, while the FZ method avoids this problem, it is more limited by geometrical and environmental constraints - its delicate set-up is only achievable in either relatively small liquid bridges under normal gravity (liquid volumes of the order of several cubic centimetres) or else in a micro-gravity environment. However, when applicable, the FZ method is often favoured, due to the aforementioned problem with the Czochralski method. Despite this, and as noted by Bänsch & Höhn (1998), flows in the liquid phase during container-free crystal production lead to inhomogeneities in dopant distribution and hence fluctuations of electrical resistivity, in the processing of doped semiconductor crystals. This motivates research for example in Cuvelier & Driessen (1986), Dold et al (1998), Kaiser & Benz (1998), Müller & Ostrogorsky (1994), Schwabe (1988), into thermocapillary and buoyancy effects on small and large-scale segregation, as surface-tension gradients at the liquid-gas interface influence the liquid motion and thermal responses. Again, related investigations of liquid bridge flows arise from interfacial phenomena in unsaturated porous media and from foam mechanics (Xu & Davis 1983). An important general conclusion drawn from the

above studies is that micro-inhomogeneities within the melt principally result from time-dependent, oscillatory buoyancy and/or thermocapillary convection, and that these, in turn, are the chief cause of undesired striations in the chemical composition of the finished crystal.

Previous efforts towards understanding and predicting the phenomena involved tend to split into direct numerical simulations, linear mathematical theory and stability analysis. There have also been some experimental studies, e.g. Chun & Wuest (1978a, 1979), Schwabe et al (1988), Velten et al (1991), but these are relatively few; a principal reason for this is that semiconductor molten is opaque for most materials considered, which naturally hinders the accurate measurement of flow properties. Another problem is caused by the difficulty in accurately applying boundary conditions, especially regarding the imposed temperature distribution of the melt surface (using for example a ring heater or mirror furnace) and on the discs (which should be maintained at equal values). Hence most of the experimental studies have tended to concentrate on the related "half-zone" problem, where the discs have different temperatures and the liquid/gas interface has zero temperature flux. This model is used as a rough approximation to the upper or lower half of the "full-zone" model, described in the previous sentence, and is mainly used to understand the instability mechanisms.

Direct simulations include those of Chun & Wuest (1978b), Clark & Wilcox (1980), Rupp, Müller & Neumann (1989), Levenstam & Amberg (1995), Bänsch & Höhn (1998), Kaiser & Benz (1998), Leypoldt, Kuhlmann & Rath (2000); some allow significant movement of the interface, and some are two-dimensional while others are three-dimensional. Again, many direct simulations have focussed on the half-zone problem, but more recent works (including the last three mentioned above) have addressed the full zone. Linear analyses assuming lubrication theory or parallel flow have been developed by Levich (1962), Birikh (1966), Yih (1968, 1969), Adler & Sowerby (1970), Babskiy et al (1973), Ostrach (1977), Sen & Davis (1982), Xu & Davis (1983), mostly for axisymmetric slender processes without end effects. Stability features, which are not directly relevant to the present study, have been investigated in various regimes by Smith & Davis (1983a,b), Xu & Davis (1984, 1985), Davis (1987), Wanschura, Kuhlmann & Rath (1997), Riley & Neitzel (1998), Nepomnyashchy et al (2001) and others.

The motivation for this paper is that clearly numerous major features in liquid crystal behaviour are thoroughly nonlinear as well as nonparallel in nature. In consequence the concern here is in direct simulations but allied with nonlinear theory. We address the steady axisymmetric setting as a starting point and include end effects. The aim also is to identify controlling parameters during the nonlinear investigation.

The finite element computations and nonlinear analysis to be described, with the latter being especially useful for slender configurations, focus on the

low Prandtl number regime where the temperature field has impact on the velocity field but effectively not vice versa. This choice reflects the nature of typical semiconductor materials; for example, the Prandtl numbers for silicon (Si), molybdenum (Mo) and gallium arsenide (GaAs), three commonly used materials, are 0.027, 0.025 and 0.068 respectively. The computations and analysis in practice were performed hand-in-hand. The effects of the aspect ratio of the configuration and of the Marangoni and Rayleigh numbers relative to the Prandtl number are of concern here. The role of the endwalls in causing the fluid motion which is mostly from hot to cold along the interface to be opposed by that along the axis of symmetry can then be examined quantitatively.

Section 2 below presents the full unsteady problem followed by the low Prandtl number version for the nonlinear steady states which are of present concern. Section 3 describes the method and results of direct numerical simulations on the governing equations, showing various cases to cover the dependence on aspect ratio, Marangoni and Rayleigh numbers and highlighting the interesting and puzzling properties. These include high shears and jet-like convection behaviour in certain regimes, together with a 'lemonhead' process which is observed in the development of bell shaped local velocity profiles and is associated with increasing the relative Marangoni effect. Wide domains of large aspect ratio are considered analytically in section 4, identifying a thermal and flow concentration towards the interfacial edge; 'wide' here in practice means aspect ratios exceeding about 2. Narrow domains with an aspect ratio which is small, below about 0.3 in practice, are examined in section 5. The flow structure then comprises a core controlled by a nonlinear slender flow balance of viscous and inviscid forces and an effectively inviscid zone near each end wall. Solutions are presented for the core, which is affected by the conditions of turning at each endwall zone as well as the effective shear force at the interface and the buoyancy force. A midway solution is also studied for relatively low Rayleigh numbers as it sheds light on the lemonhead process. The effect of increasing the Rayleigh number is included. Comparisons between the direct simulations of section 3 and the theory of sections 4,5 are made in section 6 and show good qualitative and quantitative agreement as well as confirmation of the scalings and parameters suggested analytically. An example of the latter is in the importance of the scaling of Rayleigh number with the sixth power of aspect ratio as indicated in section 5. Further comments including aspects of the nonuniqueness found theoretically are given in section 7.

2 The governing system of equations - low Prandtl numbers

We consider a finite volume of liquid suspended between two flat, rigid, coaxial discs, aligned perpendicular to the direction of gravity ($\hat{\mathbf{e}}_g$) and of equal radius, and surrounded by an ambient gas. The fluid is assumed to be at rest on the solid/liquid boundaries, while the liquid/gas interface is assumed to be

adiabatic, externally heated and time-independent, i.e. having zero normal velocity component. We further suppose that the liquid is incompressible, with dynamic viscosity ν, thermal diffusivity κ and density ρ. The temperatures on the solid/liquid boundaries are equal and maintained at the constant value T_0', while the maximum temperature on the liquid/gas interface (say T_M') is located at the mid-height of the liquid domain. The mean radius of the liquid domain R and its height d determine the aspect ratio $r_c = R/d$.

The flow is principally driven by a combination of buoyancy forces, acting globally, and thermocapillary forces, acting on the liquid-gas interface only. In obtaining a mathematical expression of the former, it is common practice to relax the incompressibility assumption, and regard density as varying with temperature. This creates an additional (Boussinesq) term in the Navier-Stokes equations, which together with the equations of mass conservation and heat transport (along with the relevant boundary and initial conditions) govern the liquid mechanics here.

Thermocapillarity arises due to the dependence of the surface tension, Σ',on the temperature, T', and enters the dynamics of the system through the equilibrium of forces on the interface. In particular, it is responsible for jumps in the shear stress and normal stress there, these being counterbalanced by the surface-tension gradient $d\Sigma'/dT'$, and the product of the surface tension and twice the mean curvature (H), respectively. For simplicity, we suppose that the surface tension has no further dependent variables (such as pressure), and is similarly unaffected by any possible concentration of foreign materials on the interface. Moreover, we employ the linear relation

$$\Sigma'(T') = \Sigma'(T_0') - \gamma(T' - T_0'), \tag{2.1}$$

which is a valid approximation provided the maximum deviation from the discs' temperature $\delta T \equiv T_M' - T_0'$ is sufficiently "small". The sign of $\gamma = -\left.\frac{d\Sigma'}{dT'}\right|_{T_0'}$ determines whether fluid is driven along the interface in the direction of *increasing* or *decreasing* temperature. In our work, γ is taken to be positive (as is true for most liquids), for which the latter feature holds true. However, the effects of negative γ in a specific theoretical context are later discussed, due to the interesting nonlinear phenomena present for that case (see sections 5.2, 7).

The scalings $d, \nu/d, d^2/\nu,\ \rho\nu^2/d^2$ and δT are used to non-dimensionalise the length, velocity, time, pressure and temperature deviation from T_0', respectively, and lead to the following form for the governing equations

$$\begin{aligned}
\tfrac{\partial \mathbf{u}}{\partial t} + (\mathbf{u}\cdot\nabla)\mathbf{u} - \Delta\mathbf{u} + \nabla p + \tfrac{Ra}{Pr} T\hat{\mathbf{e}}_g = \mathbf{0} \quad &\text{in} \quad \Omega, \\
\nabla\cdot\mathbf{u} = 0 \quad &\text{in} \quad \Omega, \\
\tfrac{\partial T}{\partial t} + (\mathbf{u}\cdot\nabla)T - \tfrac{1}{Pr}\Delta T = 0 \quad &\text{in} \quad \Omega.
\end{aligned} \tag{2.2a-c}$$

Here $\mathbf{u}$, p and T denote the dimensionless velocity, pressure and temperature fields, respectively, while Ω represents the dimensionless cavity. The associated boundary conditions are

$$\mathbf{u} = 0,\ T = 0 \ \text{ on } \ \Gamma_{SL}, \tag{2.2d}$$

$$\mathbf{u} \cdot \mathbf{n} = 0,\ T = T_D \ \text{ on } \ \Gamma_{LG}, \tag{2.2e}$$

$$\mathbf{n} \cdot \sigma \boldsymbol{\tau} = -\frac{Ma}{Pr} \nabla T \cdot \boldsymbol{\tau} \ \text{ on } \ \Gamma_{LG}, \tag{2.2f}$$

$$\mathbf{n} \cdot \sigma \mathbf{n} = 2HSt(1 - Ca\, T) \ \text{ on } \Gamma_{LG}, \tag{2.2g}$$

where $\sigma \equiv \nabla \mathbf{u} + \nabla \mathbf{u}^{\mathrm{T}} - p\mathrm{I}_3$ denotes the stress tensor, with superscript T indicating the transpose and I_3 the 3×3 identity (delta) tensor. Also here Γ_{SL}, Γ_{LG} are the solid/liquid and liquid/gas boundaries (both dimensionless), in turn, T_D is the scaled external temperature imposed on the free surface, $\boldsymbol{\tau}$ is an arbitrary vector in the local tangential plane to Γ_{LG}, and $\mathbf{n}$ is the normal vector to Γ_{LG}.

Finally, initial conditions

$$\mathbf{u} = \mathbf{u}_0,\ T = T_0 \ \text{ in } \Omega \ \text{ at } \ t = 0 \tag{2.2h}$$

are required to close the system.

A number of key parameters emerge from the above derivations, namely:

$$Ra = \frac{\beta \delta T g d^3}{\kappa \nu}, \ \ Pr = \frac{\nu}{k}, \ \ Ma = \frac{\gamma \delta T d}{\rho \nu^2}, \tag{2.3a-c}$$

$$St = \frac{\Sigma_0' d}{\rho \nu^2}, \ \ Ca = \frac{\gamma \delta T}{\Sigma_0'}, \tag{2.3d,e}$$

where β is the thermal expansion coefficient at constant pressure, and g is the acceleration due to gravity. These are, in turn, the Rayleigh number, which measures buoyancy convection in the domain, the Prandtl number, the Marangoni number, measuring thermocapillary convection on the liquid-gas interface, the surface-tension number and the capillary number, which measures the relative importance of surface-tension to its gradient in driving fluid motion at the interface.

2.1 Steady axisymmetric motion with non-deformable liquid-gas interface

If we assume that St is large, then from (2.2g) it follows that a large pressure ($0(St)$) will be induced, which, to be consistent with the hydrodynamic flow field, is hydrostatic in nature. Moreover, if $Ca \ll 1$, then again from (2.2g) the mean curvature H must be (almost) constant-valued. Consequently, we can approximate the liquid-gas interface by a non-deformable, cylindrical surface.

Further, we suppose that the fluid motion is steady, axisymmetric and two-dimensional, so that $\mathbf{u} = u(r,z)\hat{\mathbf{e}}_r + w(r,z)\hat{\mathbf{e}}_z$ in cylindrical coordinates (where the origin is defined at the centre of the lower disc and the axial coordinate vector is directed *opposite* to the gravity vector). Generally this necessitates the independence of T_D on azimuthal angle and, thus, we further suppose that $T_D = T_D(z)$. We can therefore concentrate on the flow properties in an arbitrary vertical "slice" S (defined as $(0, r_c) \times (0,1)$ in $r-z$ coordinates) of the domain (see figure 1), whereby the following equations hold,

$$u\frac{\partial u}{\partial r} + w\frac{\partial u}{\partial z} - \left[\frac{1}{r}\frac{\partial}{\partial r}\left(r\frac{\partial}{\partial r}\right) + \frac{\partial^2}{\partial z^2}\right] u - \frac{1}{r^2}u + \frac{\partial p}{\partial r} = 0 \ \text{ in } \ S, \tag{2.4a}$$

$$u\frac{\partial w}{\partial r} + w\frac{\partial w}{\partial z} - \left[\frac{1}{r}\frac{\partial}{\partial r}\left(r\frac{\partial}{\partial r}\right) + \frac{\partial^2}{\partial z^2}\right] w + \frac{\partial p}{\partial z} = \left(\frac{Ra}{Pr}\right) T \ \text{ in } \ S, \tag{2.4b}$$

$$\left(\frac{\partial}{\partial r} + \frac{1}{r}\right) u + \frac{\partial w}{\partial z} = 0 \ \text{ in } \ S, \tag{2.4c}$$

$$u\frac{\partial T}{\partial r} + w\frac{\partial T}{\partial z} - \frac{1}{Pr}\left[\frac{1}{r}\frac{\partial}{\partial r}\left(r\frac{\partial}{\partial r}\right) + \frac{\partial^2}{\partial z^2}\right] T = 0 \ \text{ in } \ S. \tag{2.4d}$$

The associated boundary conditions are

$$u = w = 0, \quad T = 0 \quad \text{on} \quad z = 0, 1, \tag{2.4e}$$

$$u = 0, \quad T = T_D(z) \quad \text{on} \quad r = r_c, \tag{2.4f}$$

$$\frac{\partial w}{\partial r} = -\left(\frac{Ma}{Pr}\right)\frac{dT_D}{dz} \quad \text{on} \quad r = r_c, \tag{2.4g}$$

$$\text{finiteness at } r = 0. \tag{2.4h}$$

2.2 High-conductivity flows ($Pr \ll 1$)

Retaining Ma/Pr and Ra/Pr as $0(1)$ parameters for now (but see subsequent sections for particular limiting cases), we apply the following simple expansions for velocity, pressure and temperature at low Prandtl number,

$$(u, w, p, T) = (u_0(r,z), \ \ w_0(r,z), \ \ p_0(r,z), \ \ T_0(r,z)) + ..., \tag{2.5}$$

where the higher-order terms first enter at $0(Pr)$ for each variable. Substituting these into (2.4a-h) yields

$$u_0\frac{\partial u_0}{\partial r} + w_0\frac{\partial u_0}{\partial z} - \left[\frac{1}{r}\frac{\partial}{\partial r}\left(r\frac{\partial}{\partial r}\right) + \frac{\partial^2}{\partial z^2}\right] u_0 - \frac{1}{r^2}u_0 + \frac{\partial p_0}{\partial r} = 0, \tag{2.6a}$$

$$u_0\frac{\partial w_0}{\partial r} + w_0\frac{\partial w_0}{\partial z} - \left[\frac{1}{r}\frac{\partial}{\partial r}\left(r\frac{\partial}{\partial r}\right) + \frac{\partial^2}{\partial z^2}\right] w_0 + \frac{\partial p_0}{\partial z} = \left(\frac{Ra}{Pr}\right) T_0, \tag{2.6b}$$

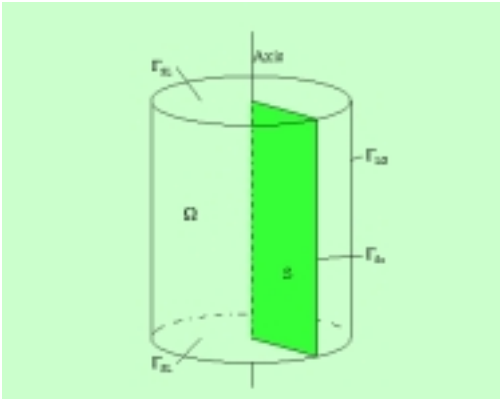

(a)

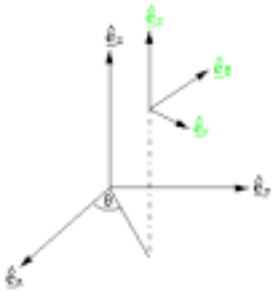

(b)

Figure 1: (a) Sketch of a cylindrical liquid-bridge domain Ω, with solid-liquid boundaries Γ_{SL} and liquid-gas interface Γ_{LG}. Axisymmetric solutions are sought in an arbitrary vertical 'slice' S (with liquid-gas interface Γ_{S_0}). (b) Cylindrical and Cartesian coordinate systems.

$$\left(\frac{\partial}{\partial r}+\frac{1}{r}\right)u+\frac{\partial w_0}{\partial z}=0, \tag{2.6c}$$

$$\left[\frac{1}{r}\frac{\partial}{\partial r}\left(r\frac{\partial}{\partial r}\right)+\frac{\partial^2}{\partial z^2}\right]T_0=0, \tag{2.6d}$$

with

$$u_0=w_0=0, \quad T_0=0 \quad \text{on} \quad z=0,1, \tag{2.6e}$$

$$u_0=0, \quad T_0=T_D(z) \quad \text{on} \quad r=r_c, \tag{2.6f}$$

$$\frac{\partial w_0}{\partial r}=-\left(\frac{Ma}{Pr}\right)\frac{dT_D}{dz} \quad \text{on} \quad r=r_c, \tag{2.6g}$$

$$\text{finiteness at } r=0. \tag{2.6h}$$

We thereby achieve a partial decoupling of the velocity and temperature fields at leading order, since, although the form of the equations controlling the hydrodynamic fields is unaltered, the velocity-dependent advection term driving the temperature is now crucially absent. We can exploit this latter feature further, by considering various possibilities for $T_D(z)$. However, we first note that $T_D(z)$ should satisfy the minimum criteria of being zero-valued on the plates, and having a maximum value of 1 at the midheight location. Another desirable and practical property is to have a symmetrical profile about $z=1/2$. Several choices based on the above criteria are available, such as parabolic or Gaussian profiles. A third possibility is a sinusoidal profile, i.e.

$$T_D(z)=\sin(\pi z) \tag{2.7}$$

which, moreover, allows us to obtain an analytical solution for the temperature: by separating variables in T_0 we can deduce from (2.6d-f,h) that

$$T_0(r,z) = \frac{I_0(\pi r)}{I_0(\pi r_c)} \sin(\pi z), \tag{2.8}$$

where I_0 is the modified Bessel function of the first kind of order zero.

Hence to leading order the complexity of the system has been reduced to that for an isothermal system, since we can now regard the buoyancy term appearing in the z-momentum equation as a known source; this feature will be further applied in sections 4,5 below. The governing equations (2.6a-h) with (2.8) are the focus for the rest of this study. For convenience we drop the suffix zero hereinafter.

3 Full computational solutions

In this section, we present solutions obtained from our full numerical simulations (DNS); these cover wide-ranging values of aspect ratio, Marangoni number and Rayleigh number, while the Prandtl number has the representative value of 0.01 unless otherwise stated. Before examining these, we first summarise the computational method that was applied.

3.1 Variational form of equations and computational method

To obtain our steady-state solutions, we addressed the full, unsteady system [(2.2a-f),(2.2h) neglecting normal stresses] using zero-valued initial data ($\mathbf{u}_0 = \mathbf{0}$, $T_0 = 0$), and ran our solver until sufficiently time-converged values of the flow variables were achieved. For the spatial discretisation, a standard Bubnov–Galerkin finite-element method was used. In order to apply this however, it was first necessary to convert (2.2a-f) into a suitable variational form, in particular one that could naturally accommodate the stress condition on the slip boundary. The following 'strain' version accomplishes this

$$\frac{d}{dt}\int_S \mathbf{u}\cdot\boldsymbol{\phi} r dr dz + \int_S D(\mathbf{u}) : D(\boldsymbol{\phi}) r dr dz + \int_S [(\mathbf{u}\cdot\boldsymbol{\nabla})\mathbf{u}]\cdot\boldsymbol{\phi} r dr dz$$

$$-\int_S p\nabla\cdot\boldsymbol{\phi} r dr dz - \frac{Ra}{Pr}\int_S T\hat{\mathbf{e}}_z\cdot\boldsymbol{\phi} r dr dz - \frac{Ma}{Pr}\int_{\Gamma_{S_0}} (\nabla T\cdot\boldsymbol{\tau})(\boldsymbol{\phi}\cdot\boldsymbol{\tau}) r ds = 0, \tag{3.1a}$$

$$\int_S (\nabla\cdot\mathbf{u})\psi r dr dz = 0, \tag{3.1b}$$

$$\frac{d}{dt}\int_S T\chi r dr dz + \int_S [(\mathbf{u}\cdot\boldsymbol{\nabla})T]\chi r dr dz + \frac{1}{Pr}\int_S \nabla T\cdot\nabla\chi r dr dz = 0, \tag{3.1c}$$

where $D(\mathbf{v}) \equiv \nabla\mathbf{v}+\nabla\mathbf{v}^T$ for any $\mathbf{v} \in C^1(\mathbf{S})$, denotes the strain-like tensor. Also here Γ_{S_0} represents the slip boundary part of S, while s is the arc length and $\boldsymbol{\tau}(s)$ the unit tangent vector (defined so that $\boldsymbol{\tau} \cdot \hat{\mathbf{e}}_z \geq 0$); for the non-deformable boundaries considered here, we clearly have $\Gamma_{S_0} = \{r_c\} \times [0,1]$, $s \equiv z$ and $\boldsymbol{\tau} \equiv \hat{\mathbf{e}}_z$.

Details behind the derivation of (3.1a-c) can be found in Bänsch (2001), Bänsch & Höhn (1998). We note that the given form is valid for 3D axisymmetric flows, but, in view of the present setting, we will focus on its 2D application. First, to eliminate the presence of singular effects in the momentum equation at $r = 0$ (evidenced for example by the strong form (2.4a)), we exploit the natural behaviour of the radial velocity component for $r \to 0$ (i.e. $u \sim r$ there) and define the (regular) function $u_\alpha := u/r$ for $r > 0$ with continuous extension to $r = 0$. Then solutions to (3.1a-c) are sought for $\mathbf{u} \in \mathbf{V} := rV^A \times V^B$, $p \in W$, and $T \in X$ such that the equations hold for all $\boldsymbol{\phi} \in \mathbf{V}$, $\psi \in W$, $\chi \in X$. Here

$$V^A := \left\{ \varphi_a : \int_S [{\varphi_a}^2 + |\nabla\varphi_a|^2] r^3 dr dz < \infty \quad \text{and} \quad \varphi_a = 0 \quad \text{on} \quad \Gamma_{S_0} \cup [0, r_c] \times \{0,1\} \right\},$$

$$V^B := \left\{ \varphi_b : \int_S [{\varphi_b}^2 + |\nabla\varphi_b|^2] r dr dz < \infty \quad \text{and} \quad \varphi_b = 0 \quad \text{on} \quad [0, r_c] \times \{0,1\} \right\},$$

$$W := \left\{ \psi : \int_S \psi^2 r dr dz < \infty \right\} \setminus \mathbb{R}$$

and $X := V^B$ (Tenhaeff 1997). The corresponding discrete velocity and temperature spaces ($:= \mathbf{V}_h \subset \mathbf{V}, X_h \subset X$, respectively) were defined by piecewise-quadratic basis functions (multiplied by a factor r in the first velocity field) and the discrete pressure space ($:= W_h \subset W$) by continuous, piecewise-linear basis functions, i.e. the Taylor–Hood triangular element was implemented. This element, fulfilling the requirements of the inf-sup stability constraint (see e.g. Brezzi & Fortin 1991, Girault & Raviart 1986), avoids any possible complications with spurious pressure modes and, as well as being relatively straightforward to implement, gives a good balance between efficiency of computation and accuracy. For this element, the velocity and temperature are of second-order spatial accuracy, while the pressure is of first-order spatial accuracy (in each case, measured relative to $L^2(\Omega)$ norm).

To discretise in time, a fractional θ-scheme with operator splitting as variant (Bänsch 1998, Bristeau, Glowinski & Periaux 1987) was applied to the hydrodynamic part coupled with a first-order, semi-implicit, backward-Euler scheme for the energy equation. To apply the former, the total timestep is first divided

into three smaller sub-steps, with the first and third using identical forms of discretisation. In the first and third step, the nonlinear convection term is treated explicitly, but implicitly in the second step; these rôles are exactly reversed for the pressure gradient, while the incompressibility constraint is relaxed in the second step. In both cases the buoyancy term is treated as a source term. The general upshot of this form of discretisation is to produce two distinct types of sub-problem: a self-adjoint, quasi-linear, Stokes system for unknown velocity and pressure; and an asymmetric, nonlinear system for velocity only. As well as full decoupling of the nonlinearity and incompressibility, the fractional θ-scheme is, moreover, virtually non-dissipative and (for self-adjoint operators) unconditionally stable.

In conjunction with spatial discretisation, the first subproblem reduced to a Schur-complement matrix equation for the pressure together with a positive-definite matrix equation for the velocity. With the former, problems with poor condition number for small time-steps (which are generally unavoidable for larger values of Rayleigh number and/or Marangoni number) make it necessary to apply a suitable preconditioner. For this purpose, the method of preconditioning described in Bristeau, Glowinski & Periaux (1987) was employed, and it proved sufficient in obtaining good (iterative) convergence speed and stability, for a wide range of Rayleigh and Marangoni numbers. Its application essentially leads to two pressure-related, positive-definite, matrix systems, both of which we solved via the method of conjugated gradients; this same method was also used to solve the velocity system. The second subproblem (as well as the fully discretised form of the energy equation) reduces to an asymmetric matrix system for velocity (temperature) only and is solved via the GMRES scheme (Saad & Schulz 1986).

3.2 Unit aspect-ratio domains

We first present results for cylinders of unit aspect ratio ($r_c = 1$), for three cases: (i) $Ra = 0$, $Ma = 1$ (ii) $Ra = 1$, $Ma = 0.1$; (iii) $Ra = 1$, $Ma = 0$. Our main concern here is to indicate the general qualitative aspects of the flow structure according to the relative sizes of the thermocapillary and buoyancy convection. First, for pure thermo-capillarity (figure 2(a)), the shear stress on the slip induces a pair of equal-sized vortices, which are symmetrically positioned about the mid-horizontal line $z = 0.5$ and rotate in opposite directions (the upper one anticlockwise). For non-zero buoyancy , the flow loses this mid-line symmetry, and, in response to increasing the Rayleigh number relative to the Marangoni number, the upper vortex expands while the lower vortex shrinks. For the medium-balanced case (ii), we obtain the flow pattern depicted in figure 2(b), while for pure buoyancy, which effectively serves as the limiting case of the aforementioned process, we find one large anticlockwise vortex filling the whole domain (figure 2(c)).

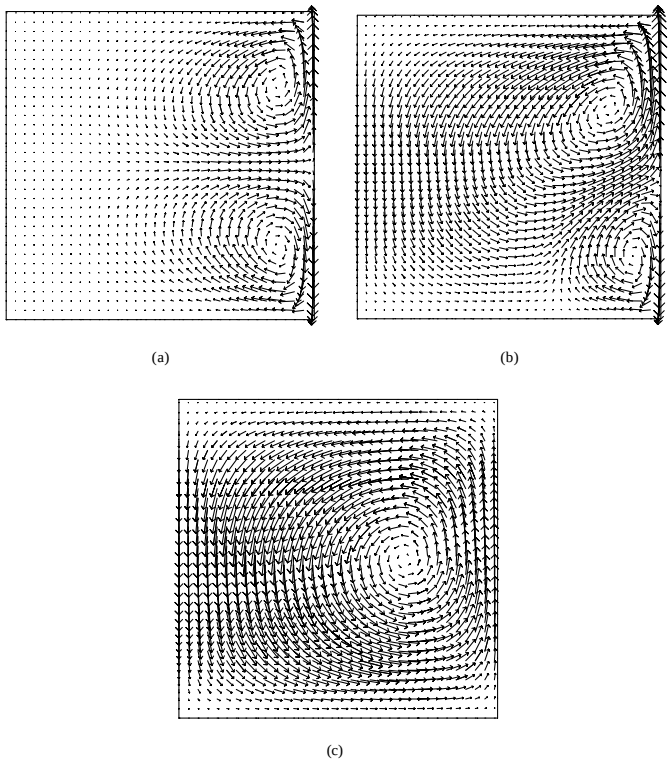

Figure 2: Computed velocity field for (a) pure thermocapillary motion ($Ra = 0$) with $Ma = 1,\ r_c = 1$; (b) combined buoyancy-thermocapillary motion with $Ma = 0.1,\ Ra = 1,\ r_c = 1$; (c) pure buoyancy motion ($Ma = 0$) with $Ra = 1,\ r_c = 1$.

Unit aspect-ratio domains were also used to validate our code, though not in the full-zone context, but for the related half-zone case. Here, we simply replaced the temperature boundary conditions from (2.4e,f) with $T = 0$ on $z = 0,\ T = 1$ on $z = 1$ and $\partial T/\partial r = 0$ on $r = r_c(= 1)$. Our code was run for a broad range of values for Ra and Ma, and compared directly with results obtained for identical cases from a finite-volume/pseudo-spectral code developed at the Center of Applied Space Technology and Microgravity (ZARM) in Bremen, Germany. Very good agreement was found in all cases tested. As a further means of validation, and as a first comparison of theoretical predictions and computation, we calculated the temperature profile on the axis for decreasing Prandtl number ($Pr = 10, 2, 1, 0.1$) for several $0(1)$ values of Ma/Pr, Ra/Pr and compared the result with the linear approximation given by (2.8), i.e. with

$$T_0(0, z) = \frac{1}{I_0(\pi)} \sin(\pi z) \quad (\approx 0.183 \sin(\pi z)). \tag{3.2}$$

There was virtually no discernible difference for Pr values as high as 0.1 in all cases tested (figure 3).

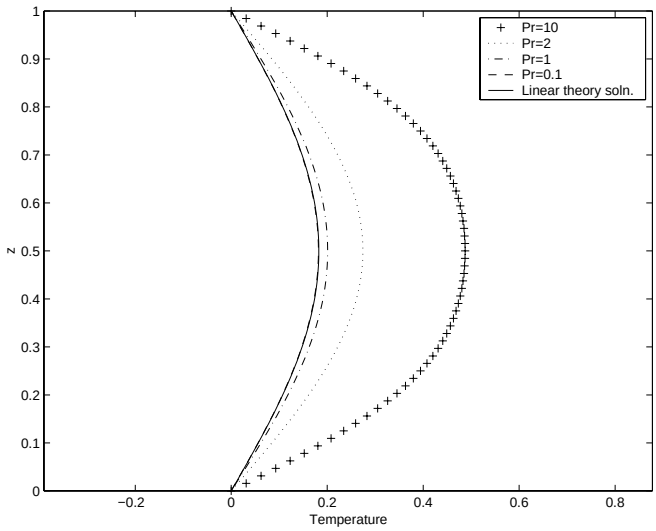

Figure 3: Temperature profile on the cylinder axis, computed for various values of Pr, with comparison against the $Pr \ll 1$ leading-order asymptotic prediction (3.2) (here $Ma = 0.01,\ Ra = 0$).

3.3 Wide-domain results

The flow properties in liquid bridges of large aspect ratio are considered here briefly. Solutions have been obtained for values of r_c in the range 2-10, for pure thermocapillary flow of various strengths. All were found to induce similar qualitative behaviour, with virtually all of the flow and thermal energy being concentrated in a box-shaped region adjacent to the slip boundary (and showing the characteristic structure of pure Marangoni convection there, as explained in the previous subsection), and thereby rendering a long, inner passive zone extending to the axis. For brevity, we refrain from reproducing all of these results here but instead focus on two cases for fixed Marangoni number ($Ma = 0.002$), with $r_c = 3$ and $r_c = 5$. Firstly, figure 4 reflects the properties just mentioned for both cases, with the features clearly defined in both cases. In figures 5a,b, a quantitative description of the flow behaviour for fixed $z(= 0.375)$ is given; viewed as if approaching the axis from the slip surface, the solutions start here with high shears, continue to peak values of the velocity components, then show a very rapid decay in flow speed until the long dormant zone is reached. Figure 5c indicates the corresponding thermal response, and interestingly we note that the temperature decay rate, while large, is visibly smaller in comparison to that for the flow speed. Possible reasons for this will be expressed in section 6, using the analytical predictions from section 4.

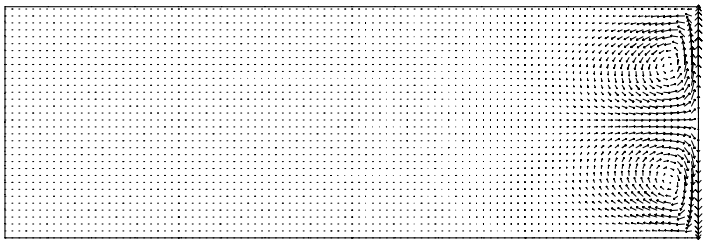

(a)

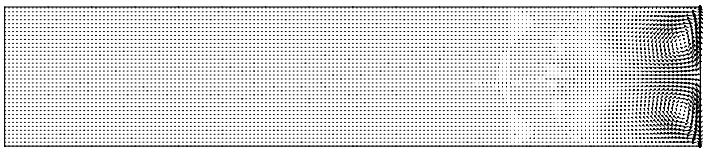

(b)

Figure 4: Computed velocity field in a wide domain for $Ma = 0.002$, $Ra = 0$ with (a) $r_c = 3$; (b) $r_c = 5$.

3.4 Narrow-domain results

Our interest here is twofold: first, to examine the flow structure for pure thermocapillary motion ($Ra = 0$) for a full range of Marangoni numbers (but small enough to produce 2D motion); and second, to investigate combined buoyancy-thermocapillary motion, again for widely varying Marangoni and Rayleigh numbers, in order to assess their relative importance on the flow structure with domains of this type. In both cases, values of r_c less than around 0.3 were deemed small enough to approximate the corresponding $r_c \ll 1$ theory (see section 5) with sufficient accuracy. For brevity, we focus on the computations performed for $r_c = 0.1$ only.

Pure thermocapillarity

For this case, we were interested in tracking the flow response for successively larger values of Marangoni number, in an attempt to detect any significant changes in the flow pattern. Results are presented here for $Ma =$ 0.1, 1, 10, 20, 30, 40, 50 and 100. We concentrate on the hydrodynamic flow developments, since the temperature in the domain is virtually independent of Marangoni number, due to the negligible feedback from velocity (via advection) with low Prandtl number fluids. Moreover, and as confirmed below in section 5.1, radial variations of temperature are now small, so that the temperature in the whole domain can be approximated by its assigned value on the slip boundary (i.e. $\sin(\pi z)$). For a more in-depth understanding, as well as providing confirmation of the accuracy of our computations, we include some plots of the linear approximation of the lubrication-limit case of (2.6a-c,e-h), detailed

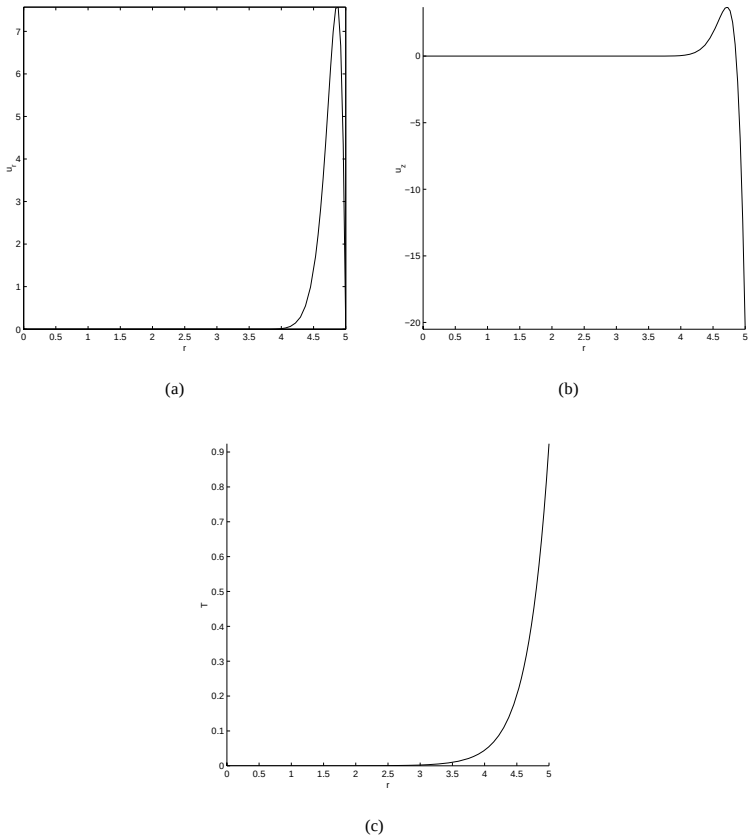

Figure 5: Wide-domain flow simulation for $Ma = 0.002$, $Ra = 0$, $r_c = 5$ depicting the profiles at $z = 0.375$ for (a) the radial velocity component; (b) the axial velocity component; (c) the temperature.

in section 5.1 below. As is described there, the *effective* size of the Marangoni convection is reduced by a factor of r_c^3 (owing to strong radial gradients of the velocity) for narrow domains, and should therefore be borne in mind here - it explains, in particular, why 2D axisymmetric motion is preserved for seemingly 'large' values of Ma/Pr. In addition to linear theory, some of our full numerical results are compared with those obtained by our finite-difference, nonlinear slender-flow solver (also described in section 5.1).

Viewed globally, the cases considered show little qualitative difference. As illustrated in figure 6 (for which $Ma = 1$), we essentially obtain a vertically-elongated version of figure 2(a), i.e. a pair of vertically-aligned, equal-sized vortices rotating in opposite directions (the upper one anti-clockwise). To examine the dynamical development with more scrutiny, we analyse the behaviour

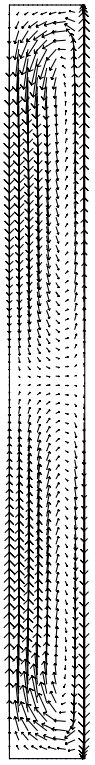

Figure 6: Computed velocity field in a narrow domain for $Ma = 1,\ Ra = 0,\ r_c = 0.1$.

of the components of velocity along both the mid-vertical line ($r/r_c = 0.5$) and the horizontal line defined by $z = 0.375$. (The latter was chosen instead of 0.5 - an otherwise more logical choice, perhaps, being at the maximum distance from a solid boundary, where linear theory is invalid - owing to the fact that the axial velocity component is zero-valued there, and would therefore have been of little use for comparison purposes.)

Figure 7 gives a comparison for the smallest values of the Marangoni number to be examined ($Ma = 0.1, 1$) and indicates very good agreement with the linear lubrication approximation. Here, as with the remaining plots, the computed velocity components have been scaled (see section 6), according to the lubrication predictions of section 5.1. Next, we reveal the plots for $Ma = 10$, 20 and 30 (figure 8) and also here display the linear approximation, in order to indicate the anticipated departure from this solution as Ma is increased. In fact, much to our surprise, the linear theory is still remarkably accurate here away from the end walls ($|z - 0.5| < 0.3$ approx.); again we refrain from further discussion until section 6.

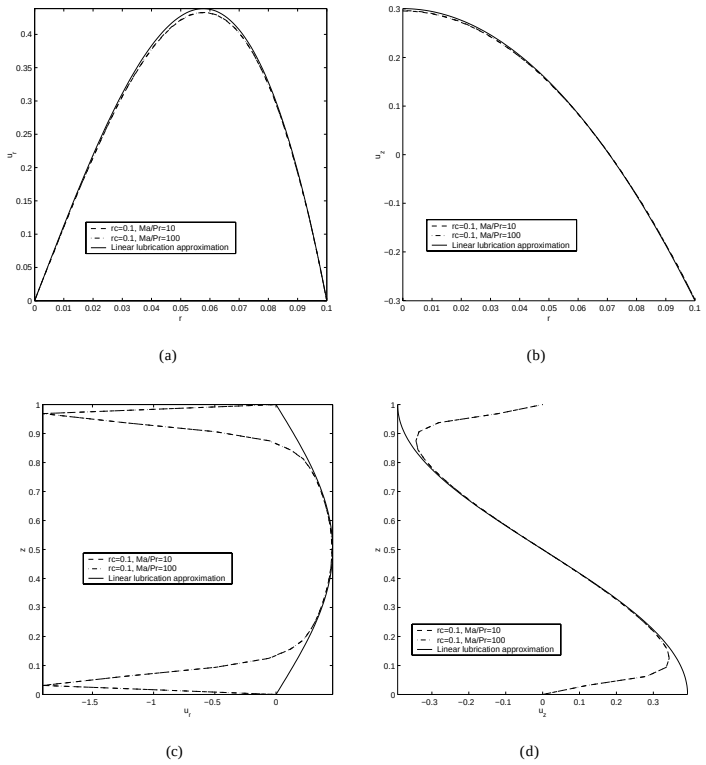

Figure 7: Narrow-domain flow simulation for $Ma = 0.1,\ 1$ with $Ra = 0$, $r_c = 0.1$, depicting the radial profiles at $z = 0.375$ for (a) the radial velocity component; (b) the axial velocity component; and the axial profiles at $r = 0.05$ for these same quantities [(c),(d), respectively]. The computed velocity components have been scaled according to (6.1a,b).

Next, the plots for the remaining Marangoni numbers are shown in figure 9, where, additionally, the case $Ma = 30$ is repeated to provide a sense of continuity and perspective with the previous figures. A number of striking features emerge from these, most notably the formation of a localised, bell-shaped, or 'lemonhead', profile for the radial velocity component around the mid-horizontal line (figure 9c). This is indicative of a strong, jet-like flow developing about $z = 0.5$, and to gain a deeper insight into the underlying mechanisms involved, we examine the flow development around $z = 0.5$ in an analytical setting in section 5.2 below. A second noticeable feature (from this same graph) is the presence of high shears on the solid boundaries. This reflects the presence of short inviscid zones, sandwiched between the bulk of the domain and the end walls. It is the viscous retardation effect of the latter which eventually dampens this high-shear behaviour. A third point (related to the first) is the large gradient of the axial velocity component near $z = 0.5$, signifying the emergence of a jump discontinuity, there (figure 9d). This is

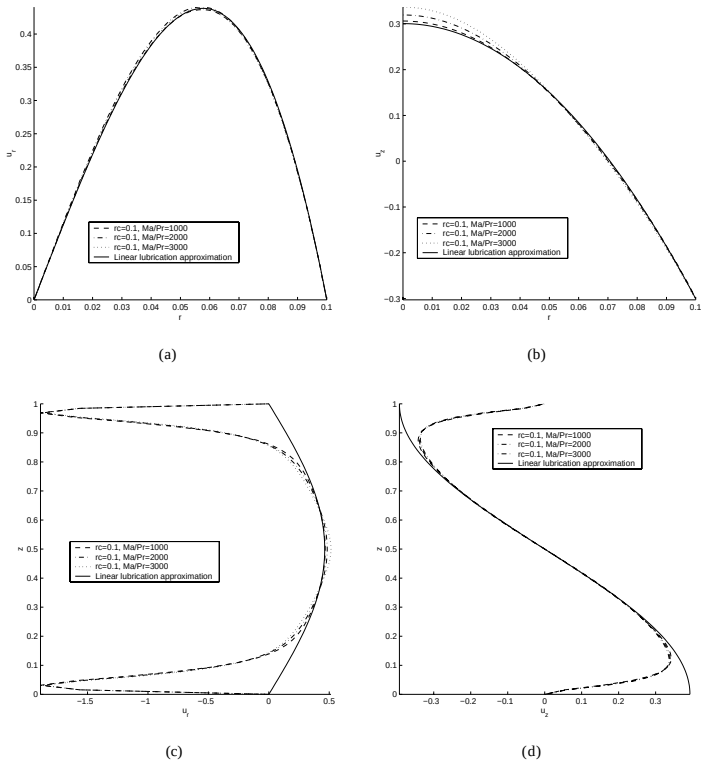

Figure 8: Narrow-domain flow simulation for $Ma = 10$, 20, 30 with $Ra = 0$, $r_c = 0.1$, depicting the radial profiles at $z = 0.375$ for (a) the radial velocity component; (b) the axial velocity component; and the axial profiles at $r = 0.05$ for these same quantities [(c),(d), respectively]. The computed velocity components have been scaled according to $(6.1a,b)$.

again clarified via the analysis of section 5.2. Once more we note here the remarkable continued accuracy of the lubrication theory in much of the domain, even for relatively large Marangoni numbers which would normally render the theory invalid.

Finally, in figure 10, we show the comparison for the case $Ma = 30$ between results obtained using our full numerical solver, and those obtained using a nonlinear slender-flow code described in section 5, where very encouraging agreement is obtained in the region of validity for the latter (i.e. away from the end walls).

Combined buoyancy-thermocapillary convection

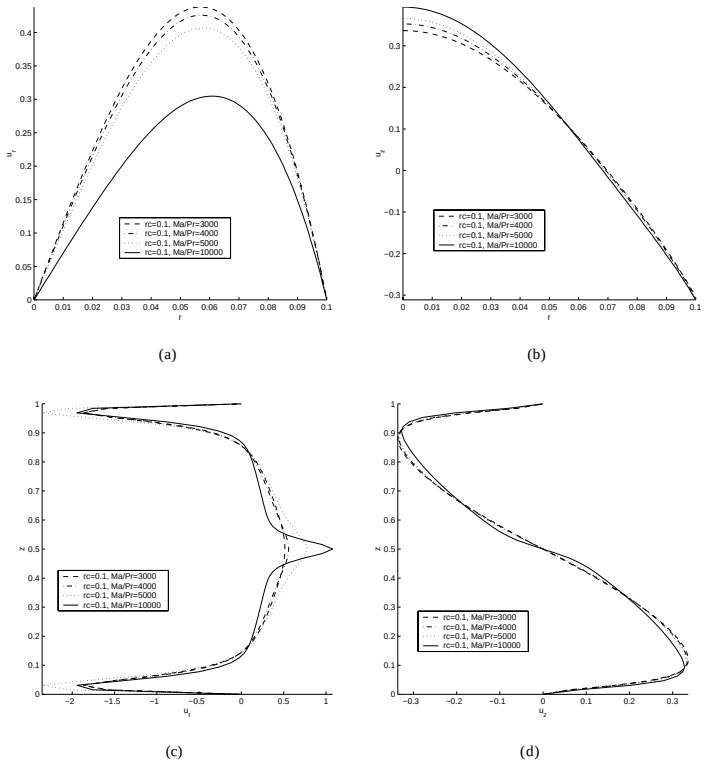

Figure 9: Narrow-domain flow simulation for $Ma = 30, 40, 50, 100$ with $Ra = 0$, $r_c = 0.1$, depicting the radial profiles at $z = 0.375$ for (a) the radial velocity component; (b) the axial velocity component; and the axial profiles at $r = 0.05$ for these same quantities [(c),(d), respectively]. The computed velocity components have been scaled according to (6.1a,b).

The effect of non-zero buoyancy is now addressed. Results are given for six cases: (i) $Ma = 0.1$, $Ra = 10^2$, (ii) $Ma = 0.1$, $Ra = 10^3$; (iii) $Ma = 0.1$, $Ra = 10^4$; (iv) $Ma = 1$, $Ra = 10^3$; (v) $Ma = 10$, $Ra = 10^4$; (vi) $Ma = 10$, $Ra = 10^5$. We note the use of large Rayleigh numbers here again stems from the small aspect ratio, as described for Marangoni numbers above. Moreover (and as described qualitatively in section 5.1 below), radial variations of the temperature are small, enabling the pressure to absorb the main buoyancy effect - hence, the effective Rayleigh number is decreased by an order of magnitude. Again, we include computed values from the nonlinear slender-flow solver for some of the graphs.

In figure 11, we present the velocity vectors in the whole plane for the first three cases. The results suggest a similar sequence of structural changes in the flow pattern when increasing buoyancy relative to thermocapillarity, as that for unit domains, i.e. the gradual filling of the whole domain by the upper vortex

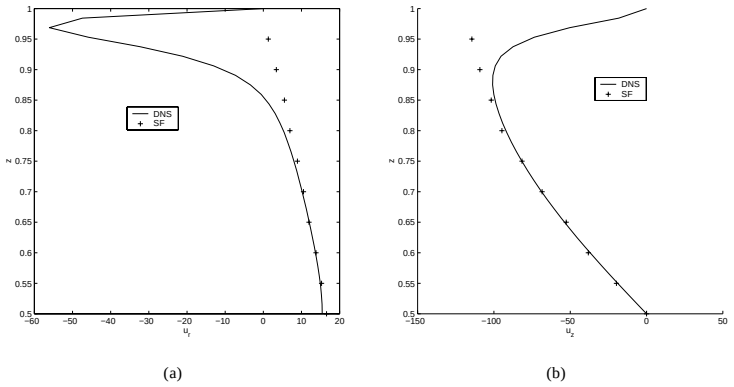

(a) (b)

Figure 10: Narrow-domain computational results for $Ma = 30$, $Ra = 0$, $r_c = 0.1$, obtained by direct numerical simulation (DNS) and nonlinear slender-flow simulation (SF). The axial profiles at $r = 0.05$ for $z \in [0.5,\ 1]$ are depicted for (a) the radial velocity component; (b) the axial velocity component.

and simultaneous shrinkage of the lower one.

The behaviour of the velocity components in the planes $r/r_c = 0.5$ and $z = 0.375$ are next depicted in figure 12, for these same cases. Here again, we use the lubrication theory as our basis for scaling the velocity components, and retain this, even for strongly-driven flows (including (vi), for example) for the sake of consistency, as well as to give some idea of the effective range of applicability of lubrication theory. The qualitative difference between these three cases is again reflected in figure 12, notably for axial velocity variations in the radial direction (figure 12b) and for radial velocity variations in the axial direction (figure 12c) - this is consistent with strong variations in the distribution of vorticity in the domain for different Rayleigh numbers (with Ma fixed), a feature consistent with figure 11. Values from the nonlinear slender-flow solver are included in figure 12 and compare very favourably with the full simulations.

In figure 13 we observe the radial/axial variations of velocity in the given planes for the fourth case, where stronger thermocapillarity is now present. The results for case (i) are repeated here, not only to serve as a guide for the relative strength of the flow produced by case (iv), but also to demonstrate the qualitative and (in scaled form) quantitative closeness of these two cases. Figure 14 then exhibits the corresponding results obtained for the strongest given capillarity (cases (v) and (vi)). Although not reproduced on the same diagrams, it is evident from figure 12 that these cases produce similar results qualitatively and quantitatively (relative to the lubrication scalings) similar to case (i) and case (ii) in turn. The quantitative similarity for the latter is somewhat more surprising, we note, given that buoyancy is significantly active here, but just seems to emphasise the fact that lubrication theory can continue to exert a strong influence on the flow structure up to and including 0(1) values

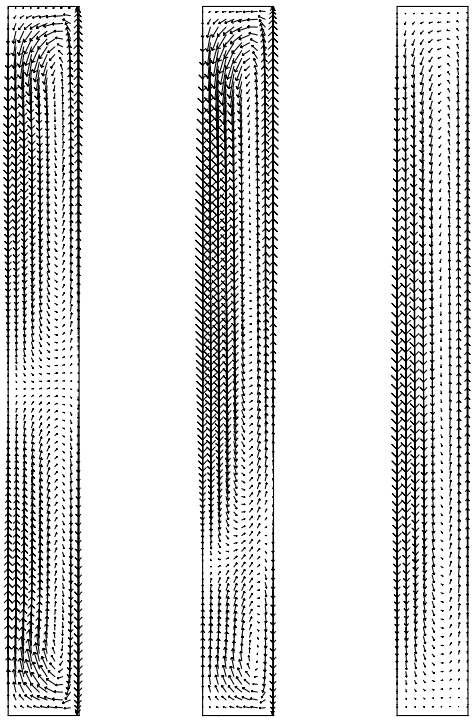

Figure 11: Computed velocity field in a narrow domain for (a) $Ma = 0.1$, $Ra = 100$, $r_c = 0.1$; (b) $Ma = 0.1$, $Ra = 10^3$, $r_c = 0.1$; (c) $Ma = 0.1$, $Ra = 10^4$, $r_c = 0.1$.

(that is 0(1) relative to the scaled system - see section 5). Finally, in figure 15 we show the axial component of velocity evaluated on (a) the slip and (b) the axis, for case (iv). Here, the predicted lubrication values (see section 5.1) are included for comparison, and excellent agreement is obtained within the region of validity (away from the end walls).

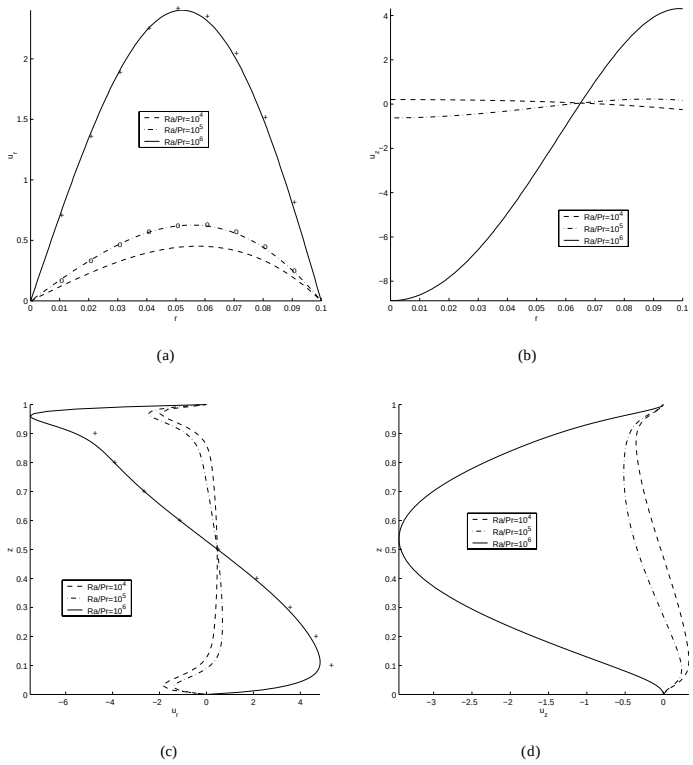

Figure 12: Narrow-domain flow simulation (DNS) for $Ra = 100,\ 10^3,\ 10^4$ with $Ma = 0.1,\ r_c = 0.1$, depicting the radial profiles at $z = 0.375$ for (a) the radial velocity component; (b) the axial velocity component; and the axial profiles at $r = 0.05$ for these same quantities [(c),(d), respectively]. Computed slender-flow (SF) data is also shown in (a) for $Ra = 10^3$ ('o') and for $Ra = 10^4$ ('+') and in (c) for $Ra = 10^4$ ('+'). The computed velocity components have been scaled according to (6.1a,b).

4 Analysis for wide domains (large r_c)

The numerical solutions of the previous section at increasing r_c values point to a relatively simple flow structure holding for a wide domain. When $r_c \gg 1$ all the major flow and thermal activity is concentrated in a 'square' zone near the edge $r = r_c$, such that

$$r = r_c + \hat{r} \tag{4.1a}$$

with $\hat{r}$ of 0(1) and

$$(w, u, p) \sim 1. \tag{4.1b}$$

It is assumed that all other parameters here are of order unity. The resulting controlling equations are the quasi-planar Navier-Stokes system

$$\partial u/\partial \hat{r} + \partial w/\partial z = 0, \tag{4.2a}$$

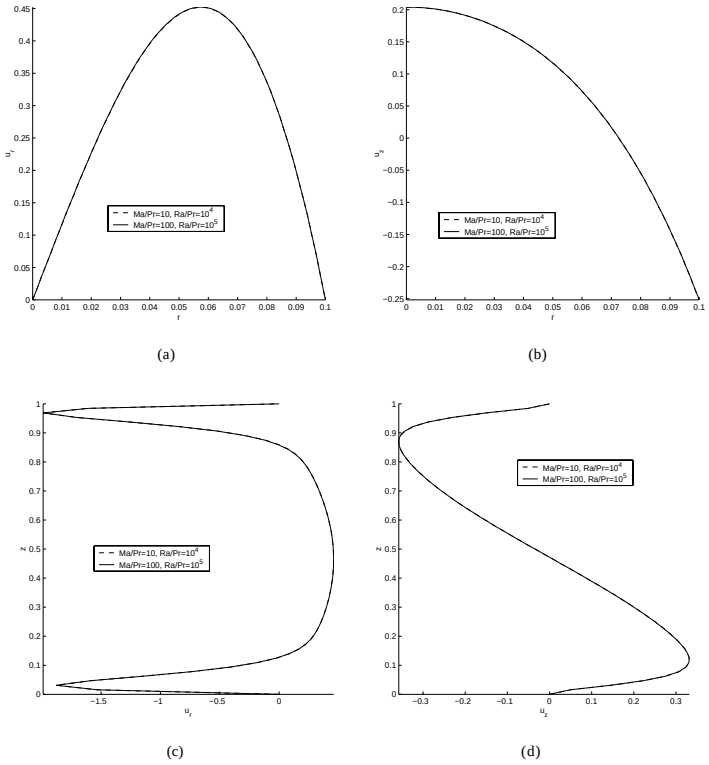

Figure 13: Narrow-domain flow simulation for $Ma = 0.1$, $Ra = 100$ and for $Ma = 1, Ra = 10^3$, both with $r_c = 0.1$, depicting the radial profiles at $z = 0.375$ for (a) the radial velocity component; (b) the axial velocity component; and the axial profiles at $r = 0.05$ for these same quantities [(c),(d), respectively]. The computed velocity components have been scaled according to $(6.1a,b)$.

$$u\partial w/\partial \hat{r} + w\partial w/\partial z = -\partial p/\partial z + (Ra/Pr)T + (\partial^2 w/\partial \hat{r}^2 + \partial^2 w/\partial z^2), \quad (4.2b)$$

$$u\partial u/\partial \hat{r} + w\partial u/\partial z = -\partial p/\partial \hat{r} + (\partial^2 u/\partial \hat{r}^2 + \partial^2 u/\partial z^2), \quad (4.2c)$$

subject to the boundary conditions

$$u = 0, \partial w/\partial \hat{r} = -(Ma/Pr)\pi \cos(\pi z) \text{ at } \hat{r} = 0, \quad (4.3a)$$

$$u = w = 0 \text{ at } z = 0, 1, \quad (4.3b)$$

$$u, w \to 0 \text{ as } \hat{r} \to -\infty. \quad (4.3c)$$

Here (4.2a-c) stem directly from (2.6a-c) and (4.3a,b) from (2.6e-g), whereas (4.3c) is a matching condition based on an assumed negligible flow at smaller radii in the majority of the domain. Again, the temperature T in (4.2b) is given by

$$T(\hat{r}, z) = e^{\pi \hat{r}} \sin(\pi z) \quad (4.4)$$

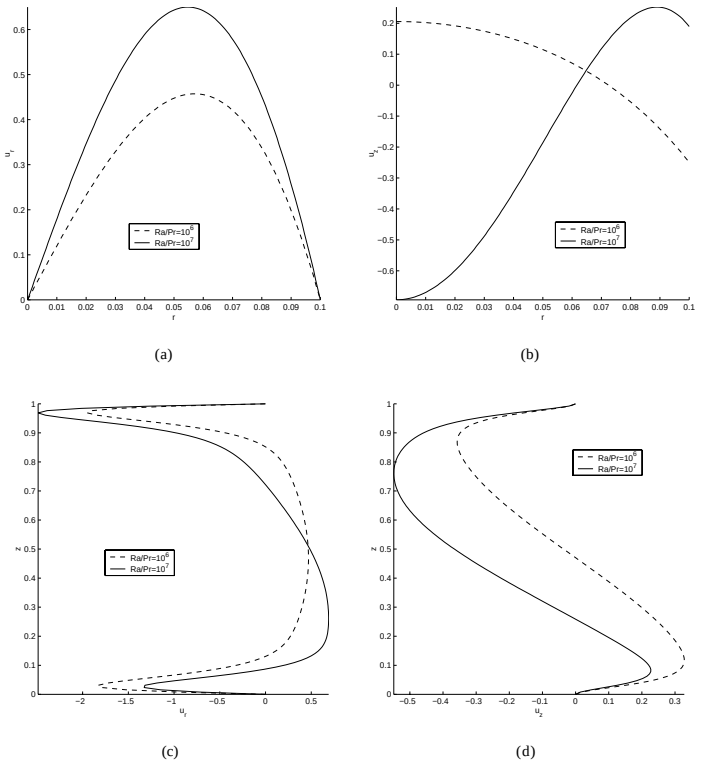

Figure 14: Narrow-domain flow simulation for $Ra = 10^4,\ 10^5$ with $Ma = 10$, $r_c = 0.1$, depicting the radial profiles at $z = 0.375$ for (a) the radial velocity component; (b) the axial velocity component; and the axial profiles at $r = 0.05$ for these same quantities [(c),(d), respectively]. The computed velocity components have been scaled according to (6.1a,b).

from (2.8) at leading order.

Under negligible buoyancy, the decaying behaviour associated with the condition (4.3c) takes the form

$$w \sim e^{\lambda \hat{r}} w^*(z) \tag{4.5}$$

provided that the real part of the unknown constant λ is positive, and similarly for u, p, as $\hat{r} \to -\infty$. So the inertia terms have little role there and, from solving for w^*, the eigenrelation

$$\lambda = \pm \sin \lambda \tag{4.6a}$$

of Stokes flow in a channel holds. The dominant decay is due to the root of (4.6a) with smallest part, which is

$$\lambda = 3.98804 + 1.63511i \tag{4.6b}$$

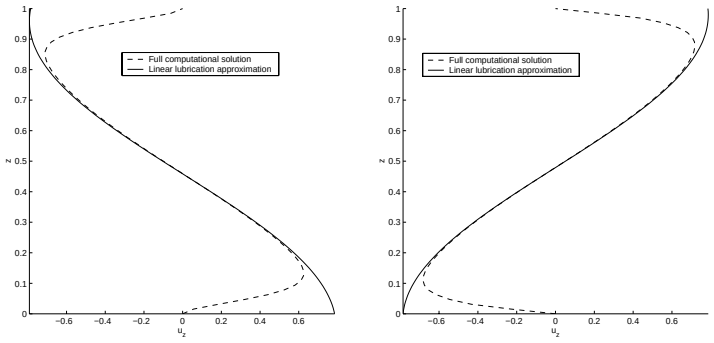

Figure 15: Narrow-domain computational results for $Ma = 1$, $Ra = 10^3$, $r_c = 0.1$, depicting the axial profile of the axial velocity component on (a) the axis ($r = 0$); (b) the slip boundary ($r = 0.1$). Corresponding theoretical profiles obtained from the linear lubrication approximation (see at end of section 5.1) are included for comparison. The computed velocity components have been scaled according to (6.1a,b).

and comes from the minus sign in (4.6a). By contrast a root $7.31440 + 2.12903$i is the one with smallest real part when the plus sign is taken.

In the presence of buoyancy the thermal forcing produces a spatial decay rate which is slower, such that in effect

$$\lambda = \pi \tag{4.6c}$$

in view of (4.4).

These results along with the predictions in the next section will be compared in section 6 with the full computations of section 3, but we note in passing that the e-folding distance of approximately $1/4$ inferred from (4.6b) would tend to suggest application of the wide-domain analysis for r_c values greater than about 2 say.

5 Analysis for narrow domains (small r_c)

Again in line with the computational results of section 3, here for sufficiently large Ma/Pr the motion is expected to be characterised by a nonlinear viscous-inviscid slender-flow region occupying almost all of the narrow domain and two end regions which are mainly inviscid, as follows.

5.1 Flow structure

In the slender flow (or boundary layer) region for $0 < z < 1$ the representative $r \sim r_c$ is small and so a nonlinear inertial balance is typified by $w\partial w/\partial z \sim \partial^2 w/\partial r^2$, suggesting that $w \sim r_c^{-2}$. This gives $\partial w/\partial r$ of order r_c^{-3} which should be compared with Ma/Pr in view of (2.6g). Similar reasoning raises the possibility that Ra/Pr being of order r_c^{-4} should be of prime concern, since then the buoyancy force $(Ra/Pr)T$ in (2.6b) with T of 0(1) is comparable with the dominant inertial force which is known to be of order r_c^{-4} from the inertial-viscous balance just described. When r_c is small however the temperature T becomes independent of r at the first approximation, and hence equal to $\sin(\pi z)$ for all r, owing to the overwhelming r-derivatives in (2.6d) (and see (2.8)); such a thermal effect uniform in the cross section can be absorbed into the main pressure gradient as the latter is also uniform in the cross section and in consequence there is no buoyancy effect produced on the flow in that case. Instead, the temperature correction of order r_c^2, which is radially dependent, must be brought into play (where $T = \sin(\pi z) + r_c^2 \overline{\overline{T}}(r/r_c, z) + \cdots$, say), in order to influence the main governing balance, and that invokes a scaling of Ra/Pr with $0(r_c^{-6})$. The very large size of this scaling for Ra/Pr is particularly noteworthy.

The velocity and pressure then are expressed at leading order by

$$(u, w) = (r_c^{-1}\bar{u},\ r_c^{-2}\bar{w}),\ \text{with } r = r_c\bar{r}, \tag{5.1a}$$

$$p = -r_c^{-6}\overline{Ra}\pi^{-1}\cos(\pi z) + r_c^{-4}(\bar{p} + \hat{\bar{\pi}}(z)), \tag{5.1b}$$

pointing from (2.6b,c) to the controlling equations

$$\partial(\bar{r}\bar{u})/\partial\bar{r} + \bar{r}\partial\bar{w}/\partial z = 0, \tag{5.2a}$$

$$\bar{u}\partial\bar{w}/\partial\bar{r} + \bar{w}\partial\bar{w}/\partial z = -\bar{p}'(z) + \overline{Ra}\overline{\overline{T}}(\bar{r}, z) + \bar{r}^{-1}\partial(\bar{r}\partial\bar{w}/\partial\bar{r})/\partial\bar{r}. \tag{5.2b}$$

The effective pressure gradient here is independent of $\bar{r}$ in view of the radial momentum balance. The scaled stream function ψ implied by (5.2a) satisfies $\bar{r}\bar{u} = \partial\psi/\partial z$, $\bar{r}\bar{w} = -\partial\psi/\partial\bar{r}$ and $\psi = 0$ at the axis $\bar{r} = 0$. The boundary conditions on (5.2a,b) are

$$\bar{u} = 0,\ \partial\bar{w}/\partial\bar{r} = -(AM)\pi\cos(\pi z) \quad \text{at} \quad \bar{r} = 1, \tag{5.2c,d}$$

$$\text{finiteness at } \bar{r} = 0. \tag{5.2e}$$

Here AMdenotes the scaled dynamic Reynolds number or forcing amplitude given by

$$AM \equiv r_c^3(Ma/Pr), \tag{5.3a}$$

in view of (2.6g). We shall see below that AM being of order one turns out to define a crucial parameter regime. Further here

$$Ra/Pr = r_c^{-6}\overline{Ra} + ..., \text{ and } \overline{\overline{T}}(\bar{r}, z) = \tfrac{1}{4}\pi^2(\bar{r}^2 - 1)\sin(\pi z) \tag{5.3b,c}$$

where the representative value of $\overline{Ra}$ is taken as $0(1)$ while the form of $\bar{\bar{T}}$ follows from (2.8). The extra absorbed pressure term in (5.1b) is defined by $\hat{\bar{\pi}}(z) = -\left(\overline{\overline{Ra}}/\pi\right)\cos(\pi z)$ if an $r_c^{-4}\overline{\overline{Ra}}$ contribution is added to (5.3b), and so on. The nonlinear slender flow equations (5.2a,b) are also subject to 'reflection' conditions at the ends, in the form

$$\bar{w}(\psi) = -\bar{w}(\psi) \text{ at } z = 0+, \quad z = 1- . \tag{5.4}$$

The argument for (5.4) relies on the motion inside the end region at $z = 1$ say, which is nonlinear and inviscid because of the shortened z scale there and hence is governed by the Euler equations. This z scale is of order r_c such that $\hat{z} = (z-1)/r_c$ is of $0(1)$, and mass conservation implies that u rises to order unity in the end region and the pressure variation is also of order unity. Accordingly the vorticity and the Bernoulli head $p+(u^2+w^2)/2$ remain unchanged along each streamline. If we combine that with mass conservation and an assumption of no substantial separation arising inside the end region, so that a tangential flow condition applies at $\bar{r} = 0, 1$ and at $\hat{z} = 0$, then the result (5.4) follows since at large negative $\hat{z}$ the flow becomes unidirectional ($u \to 0$) and the pressure becomes constant, leaving $w^2(\psi)$ conserved. Thus the two sides in (5.4) correspond to the inflow and outflow parts of the end profiles. The argument applies similarly at the end $z = 0$. We remark here that ψ is zero at $\bar{r} = 1$ as well as at $\bar{r} = 0$ due to the total mass conservation. The assumption of substantially separation free flow within the end region is in keeping with the absence of no-slip surfaces except along the endwall boundary $\hat{z} = 0$ which is the most likely position for any separation, the assumption is also in line with the computations of the previous section, and it seems reasonable at least in the current range of parameters.

Computations of (5.2a-e),(5.4) were performed by repeated finite difference sweeping of the flowfield, lagging the nonlinear terms at each sweep so as to produce in effect a forced lubrication problem at each sweep and then iterating to convergence. Each sweep thus involved repeated integration of the lagged $\bar{u}\partial\bar{w}/\partial\bar{r} + \bar{w}\partial\bar{w}/\partial z$ terms with respect to $\bar{r}$ to obtain unlagged $\bar{u}, \bar{w}$ updates and determine the pressure gradient satisfying (5.2c-e). We observe that, similarly to the features in section 3, finiteness requires $\bar{u}$ to be $0(\bar{r})$ and $\bar{w} - \bar{w}(0,z)$ to be $0(\bar{r}^2)$ as $\bar{r}$ tends to zero. Upwind differencing was applied to those lagged terms and proved stable and accurate for sufficiently fine grids such as those adopted for the results shown in the figures below. The reflection condition (5.4) was treated by using the outflow part of the $\bar{w}$ profile calculated at $z = 0$ or $z = 1$ to generate monotonically increasing or decreasing ψ values there, and hence update the $\bar{w}(\psi)$ function, and then applying $-\bar{w}(\psi)$ to determine the corresponding inflow part of the profile, exactly consistent with the total mass conservation.

For sufficiently low forcing, i.e. small AM and $\overline{Ra}$, the results agree generally, although subject to at least one exception, with lubrication theory as might be

expected. Thus

$$\bar{w} = \frac{\bar{r}^2}{4}\bar{p}'(z) - \alpha\left(\frac{\bar{r}^4}{16} - \frac{\bar{r}^2}{4}\right)\sin(\pi z) + b(z),$$
$$\bar{u} = -\frac{\bar{r}^3}{16}\bar{p}''(z) + \alpha\pi\left(\frac{\bar{r}^5}{96} - \frac{\bar{r}^3}{16}\right)\cos(\pi z) - b'(z)\frac{\bar{r}}{2},$$
$$\bar{p}'(z) = -2(AM)\pi\cos(\pi z) - \frac{\alpha}{2}\sin(\pi z), \quad b(z) = -\frac{p'(z)}{8} - \frac{5\alpha}{48}\sin(\pi z), \tag{5.5a-d}$$

where $\alpha \equiv \pi^2\overline{Ra}/4$. We remark that the reflection condition (5.4) is satisfied as well here. The reference above to an exception is explained a few paragraphs further on.

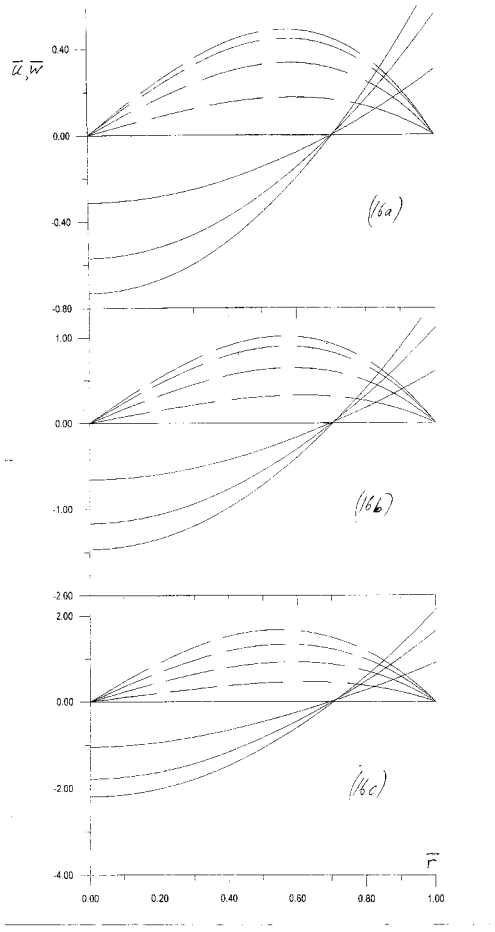

Figure 16: (a) Scaled velocity profiles for $AM = 1$, $\overline{Ra} = 0$ showing $\bar{u}$ vs. $\bar{r}$, dashed, and $\bar{w}$ vs. $\bar{r}$, solid; from top to bottom respectively (in the left part of the figure as far as $\bar{w}$ is concerned) the curves are for $z = \frac{1}{2}, \frac{5}{8}, \frac{3}{4}, \frac{7}{8}$. This is from slender-flow (SF) theory. (b) As (a) but $AM = 2$. (c) As (a) but $AM = 3$.

5.2 Negligible buoyancy

Flow results are described first for zero $\overline{Ra}$. We sought here only solutions symmetric about the midway line $z = 1/2$, in which case the z range was restricted to $1/2$ to 1 and the symmetry condition $\bar{w} = 0$ at $z = 1/2$ was applied. In figures 16(a-c) we show results for AM values of 1 to 3. For relatively low AM the solutions comply with lubrication theory. As AM increases nonlinearity enters, a property which is clear from comparisons with a local solution to be demonstrated in subsequent figures and examined in the next paragraph. In all cases here an anticlockwise vortex is formed in the upper half of the domain where $1/2 \leqslant z \leqslant 1$. Other noteworthy points are the changes in the scale as AM is varied, the almost common radial position at which $\bar{w}$ is zero as z varies, and the further properties of these slender flow solutions given respectively in figure 18 below. It was found however that a converged solution could not be obtained at AM equal to 4 satisfying the symmetry constraint at $z = 1/2$ and indeed neither could a nonsymmetric solution be obtained.

When $\overline{Ra}$ is negligible symmetry can be assumed at the midway line (this assumption is tested later), as $z \to 1/2$, such that

$$(\bar{u}, \bar{w}, \bar{p}') = (\tilde{u}, (z - 1/2)\tilde{w}, (z - 1/2)\tilde{q}) + ..., \tag{5.6}$$

with $\tilde{u}, \tilde{w}$ unknown functions of $\bar{r}$ and $\tilde{q}$ an unknown constant. So the local form is governed by the ordinary differential system

$$(\bar{r}\tilde{u})' + \bar{r}\tilde{w} = 0, \quad \tilde{u}\tilde{w}' + \tilde{w}^2 = -\tilde{q} + (\bar{r}\tilde{w}')'/\bar{r}, \tag{5.7a,b}$$

and the boundary conditions, stemming from (5.2c-e),

$$\tilde{u} = 0, \;\; \tilde{w}' = (AM)\pi^2 \;\; \text{at} \;\; \bar{r} = 1, \tag{5.7c,d}$$

$$\text{finiteness at } \bar{r} = 0. \tag{5.7e}$$

Here the prime signifies differentiation with respect to $\bar{r}$. Numerical solutions of the nonlinear problem (5.7a-e) as AM is varied are presented in figure 17(a,b), based on abridging the computational scheme discussed earlier in this subsection but the solutions were also checked by means of a separate alternative semi-implicit iterative procedure.

In particular $\tilde{q}$ versus AM is shown in figure 17(a). Three striking features are (i) there is a positive cut-off value AML of AM equal to approximately 3.3108, (ii) two solution branches exist for all AM values at which there is a solution, (iii) (which is essentially a special case of (ii)) there are two solutions for zero AM. Sample velocity profiles are also given in figure 17(b), these demonstrating the different local solutions at one fixed AM value less than AML. In certain cases the $\tilde{w}$ and/or the $\tilde{u}$ profile is positive on one branch but negative on the other. The top branch came straight from solving for $\tilde{q}$, by

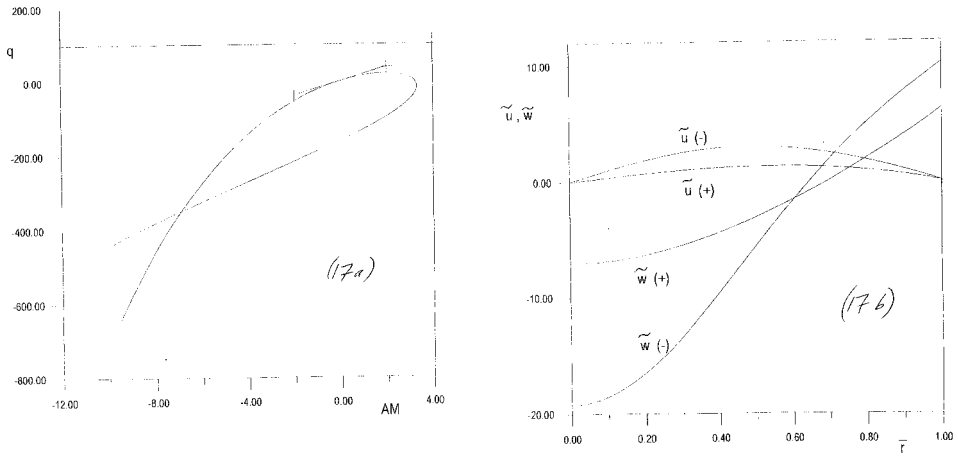

Figure 17: (a) Midway-analysis result for $\tilde{q}$ vs. AM. Lubrication result is indicated for comparison, by crosses.
(b) Scaled velocity profiles at $AM = 2.428354$: upper branch solution denoted ($+$) has $\tilde{q} = 19.92617$, lower branch ($-$) has $\tilde{q} = -80.75288$.

the way, with AM prescribed, whereas the other branch was derived by fixing a nontrivial linear combination of $AM, \tilde{q}$, not just one or the other. The feature (iii) explains our reference to "at least one exception", just before (5.5a-d). For the lubrication result (which in this setting works well only for AM below about 1) is not the only one at small AM as far as the local flow is concerned; clearly there is at least one other solution, which is nonlinear in nature. Moreover we could not find solutions for AM beyond AML, on the right. If in fact there is no solution there in the above local form we would anticipate the presence of a smaller square buffer zone surrounding the midway line, at such AM values greater than AML, a matter which is taken further in the next section. On the left, the response of the solution branches at increasingly negative AM values is interesting but is not pursued here as negative values are not directly relevant to the present context, although they are physically achievable in other contexts.

The local ordinary-differential results from (5.6)-(5.7e) also agree well numerically near $z = \frac{1}{2}$ with the earlier described computations of (5.2a-e),(5.4) as figure 18(a-c) shows for the velocity profiles at $\bar{r} = \frac{1}{2}$ and the pressure gradient. The agreement is with the top branch of the local solution and holds throughout a broad range of values of AM up to the cut-off value. In detail, for $AM = 1$ the agreement in fact extends to most z heights but for $AM = 2, 3$ it becomes confined close to the midway line and indeed for $AM = 3$ the scaled shear $\partial\bar{u}/\partial z$ varies quite rapidly and the curvature of the pressure gradient is relatively high near the midway line.

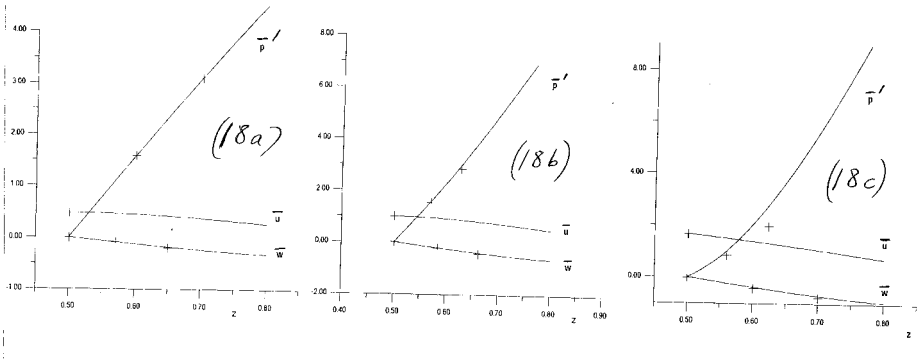

Figure 18: (a) Comparisons between global slender-flow solution (solid) and midway predictions (shown $+$) for $\bar{p}'$, and $\bar{u}, \bar{w}$ at $r = \frac{1}{2}$, vs. z. Here $AM = 1, \overline{Ra} = 0$. (b) As (a) but $AM = 2$. (c) As (a) but $AM = 3$.

5.3 Increasing buoyancy effects

For nonzero $\overline{Ra}$, we applied the same method for (5.2a-e), (5.4) but in the whole z interval of 0 to 1, since symmetry is definitely lost with $\overline{Ra}$ present. The computational results samples of which are in figure 19(a-c) show the influence of varying $\overline{Ra}$ at several AM values (or vice-versa). The solutions agree with the solutions of lubrication theory at relatively low parameter values but then nonlinearity becomes significant as $\overline{Ra}$ (or AM) increases. Here as a test all the results at small $\overline{Ra}$, for any value of AM studied, were found to tie in with those that assumed midway symmetry in the preceding subsection. As $\overline{Ra}$ increases an anticlockwise vortex gradually takes over in the majority of the flow domain. A wide variety of $\overline{Ra}$ values could be covered provided that AM was not too large; compare with section 5.2.

In more detail, figure 19(a) shows results for three cases of $(AM, \overline{Ra})$ values: $(0.1, 0.1)$ for which the buoyancy effect is seen to be small and $\bar{u}$ is nearly symmetric about the midway line; $(0.01, 0.1)$ where the nonsymmetry is increased; and $(0.01, 1)$ which appears buoyancy-dominated with $\bar{u}$ nearly antisymmetric about the midway line, the pressure gradient is nearly symmetric and the vertical velocity $\bar{w}$ is mostly negative. Other properties for these cases are given in figure 19(b), confirming the trend towards almost a single vortex as $\overline{Ra}$ increases for given AM. Figure 19(c) presents an intermediate case with increased parameter values $(1, 10)$. Some data from the slender-flow results in figure 19(a-c) was used earlier in figure 12 for comparison purposes.

6 Comparisons

Here we summarise the comparisons between direct computation (DNS) and the analysis presented in sections 4,5.

Starting with the wide-domain flow simulation, we first observe that the DNS results presented for $r_c = 3, 5$ (figures 4,5) tie in very well with the flow structure predicted in section 4, i.e. the heavy concentration of flow and thermal energy in a square zone adjacent to the interface and the subsequent long, passive inner zone. In fact this general flow pattern was discernible for aspect ratios as low as 2. It is further evident from figure 5 that the velocity components and temperature undergo a rapid decay on approach to the axis and moreover that the general decay rate for velocity is larger than that for temperature; these features are consistent with the theoretical findings of (4.4)-(4.6), where the dominant (exponential) decay constants are 3.98804 and π ($\approx$ 3.14159) respectively.

We now turn our attention to the results obtained for narrow-domain flows, beginning with those for zero buoyancy. We first comment that very good agreement between the DNS computations and the nonlinear slender-flow (SF) computations, described in section 5, was obtained for $AM \leq 3$. This can be directly seen in figures 10(a,b) (where $AM = 3$) and indirectly from inspection of figures 7,8 (DNS) and 16(a-c) (SF). The latter set of DNS figures includes comparison with the linear, lubrication predictions of (5.5a-d) with α set to zero there and emphasises the real extent to which the lubrication approximation might be reliable, since (remarkably) good accuracy within the axial interval (0.2,0.8) is obtained for AM values as high as 3 (this is despite the limited range of agreement indicated by the local results in figure 17(a)). For the purpose of making such a comparison, the computed velocity components were scaled by combining (5.1a) with (5.5a,b), i.e.

$$u \longrightarrow (r_c/AM)u, \quad w \longrightarrow (r_c^2/AM)w. \qquad (6.1a,b)$$

In the DNS plot of figure 9(c), the emergence of the 'lemonheads' from the midway zone, where the radial velocity component develops a bell-shaped profile around $z = 0.5$, becomes an increasingly prominent feature as AM is raised beyond the value of 3. Simultaneously, the axial velocity component develops a steep axial gradient there (figure 9(d)). Examination of the midway zone dynamics (section 5.2) reveals the limitations of the slender-flow approximation by pointing to a cut-off value for AM at about 3.3108, beyond which no local solutions of the same type are obtainable. This, in particular, would account for the breakdown of the SF computations at values of AM above about 3; indeed preliminary investigations seem to indicate that a square nonlinear, inviscid (Euler) zone of thickness $O(r_c)$ develops around the midway line and moreover this zone is chiefly responsible for the 'lemonhead' formation and the effective 'jump' in the axial velocity component.

The very good agreement between the DNS and the SF computations continues for problems with significant buoyancy ($\overline{Ra} \neq 0$), as figures 12-14 (DNS) and figure 19 (SF) demonstrate. A direct comparison can be seen in some instances (figure 12(a,c)), where both qualitative and quantitative agreement is

evident. Furthermore, and again somewhat surprisingly, both sets of computational results agree well with the lubrication approximation, (5.5a-d), up to and including $O(1)$ values of $\overline{Ra}$ and AM. This is directly observable in figure 15 for example, where $\overline{Ra} = 0.1$, $AM = 0.1$; here, as with figures 12-14, we have applied (6.1a,b) to scale the velocity components, while for figure 19 we applied (5.1a) only for this purpose. A related result is the qualitative and (for values of AM, $\overline{Ra}$ up to and including unity, at least) quantitative similarity for flows with a common value of $\overline{Ra}/AM$ (or equivalently Ra/Ma); this, we believe, is a direct consequence of the good lubrication approximation. Unlike the case for zero buoyancy however (or indeed for zero *effective* buoyancy where $\overline{Ra}$ is zero, but $\overline{\overline{Ra}}$ can be non-zero), we do not encounter the same slender-flow breakdown near $z = 0.5$ owing to the immediate loss of symmetry for non-zero values of $\overline{Ra}$.

The narrow-domain DNS computations displayed in this work were obtained for r_c fixed at 0.1; the flow structure found from the slender-flow analysis, however, is generally observable for values of r_c up to about 0.3.

7 Further comments

The many points of agreement found in the previous section between the direct numerical simulations and the nonlinear slender flow or boundary layer solutions are encouraging in the present setting of steady axisymmetric behaviour and supplement the strictly low amplitude predictions of lubrication solutions. This is with or without buoyancy and for narrow domains of aspect ratio r_c below about 0.3 in practice, whereas the wide domain approximation works for ratios above about 2. New features in the narrow domain case tend to put emphasis on nonlinear effects, including the end region flows, the midway response below and above the critical amplitude value AML (approximately 3.3108), the interaction of these with the global flow solution, and the various types of recirculating vortices that are induced. The end regions and the midway dynamics are mostly passive in terms of the global motion but they produce some important local properties, especially the overshoots in the radial velocity profiles within the end regions and the effective profile jumps due to the midway zone at supercritical amplitudes. In particular the 'lemonhead' phenomenon of bell-shaped profiles seen in the direct simulations is explained by the emergence of the extra Euler zone which acts as a square buffer zone between the two main halves of the axisymmetric domain and produces local overshoot profiles similar to those of the end regions. In keeping with this a related study shows that slender flow solutions for supercritical amplitudes tend to give w profiles which did not tend to zero at the midway line. With significant buoyancy present on the other hand the midway zone is eradicated and the trend towards a single main anticlockwise vortex takes precedence.

The work further suggests that a follow-up investigation on possible nonunique-

ness of the flow solution within the whole domain in the full Navier-Stokes or slender flow context would be interesting, based on the local midway ordinary-differential findings of nonuniqueness in section 5. Also study of solutions with negative AM values is worth continuing, since although not directly relevant with the current set-up, a number of practical situations exist where they could conceivably arise. Firstly, although uncommon, there are some liquids with negative-valued coefficients of surface-tension gradient γ. Secondly, for positive-valued γ, it would appear feasible in the practical setting that imperfect heating from an experimental source or even inhomogeneous heat-loss effects at the interface could lead to the scenario, where two local temperature maxima exist *either side of* $z = 0.5$, say at $z = 0.5 + \epsilon_1$ and $z = 0.5 - \epsilon_2$ (where $\epsilon_1,\ \epsilon_2$ are small and positive), with no intervening local maximum assumed. This would then effectively induce a localised 'negative AM' region inside $|z - 0.5| < \epsilon \equiv \min(\epsilon_1,\ \epsilon_2)$, due to the sign change in temperature gradient. It should be mentioned here that there may be yet more solution branches in the ordinary differential system in view of the nonlinearity acting in the midway zone.

As well as the current ranges of parameters studied there are several other ranges which are of practical interest; these include increased Prandtl number, various ranges of Ma/Pr and Ra/Pr, and the likelihood of strong wall jets appearing at higher forcing amplitudes. Significant questions need addressing on the flow stability (e.g. concerning the striations mentioned in the Introduction), on allowing for movement of the interface by an 0(1) relative amount and on three-dimensional motion.

Concerning the movement of the liquid-gas interface, for relatively small deformations an analytical form for the hydrostatic shape of the interface (valid away from the end walls) can be derived in various settings. We first recall from section 2.1 that in the regimes $St \gg 1$ and $Ca \ll 1$ a large hydrostatic pressure of $O(St)$ is induced, while the mean curvature H is approximately constant. If we further suppose that $\bar{C} \equiv St\ Ca$ is $O(1)$, then it can be inferred from (2.2g) that the interface assumes the following form:

$$R(z, r_c) = r_c[1 + St^{-1}\hat{R}(z)] + \cdots , \tag{7.1}$$

where $\hat{R}(z)$ indicates the principal scaled deformation of the interface. Moreover, it can be shown that $H \sim -1/R + O(St^{-2})$ (see e.g. Xu & Davis 1985), so that (2.2g) yields

$$\hat{R} = -r_c p/2 - \bar{C}T \quad \text{on} \quad r = r_c, \tag{7.2}$$

from the balance of 0(1) terms.

To illustrate this, we briefly consider two examples, both in the context of narrow-domain flows ($r_c \ll 1$). Firstly, for the instance where we have

significant buoyancy ($\overline{Ra} = O(1)$), we can directly determine from (5.1b) and the sinusoidal approximation for the temperature, that (to within $O(r_c^2)$)

$$\hat{R}_1 = A_1 \cos(\pi z) - B_1 \sin(\pi z) \tag{7.3}$$

for $0 < z < 1$, where $A_1 \equiv \overline{Ra}/2\pi$, and $B_1 \equiv r_c^5 \bar{C}$. Here $\hat{R}_1 = r_c^5 \hat{R} + D_1/2$ denotes the principal deformation scaled additionally in terms of r_c, and offset by a constant amount $D_1/2$, where D_1 indicates the main pressure constant of integration, stemming from (5.1b). (We note that this latter feature has no important effect on the deformation process itself, merely giving rise to a small, uniform horizontal shift of the interface.) Since A_1 is positive, we can conclude that three distinct (in a canonical sense) cases exist, these being (i) $A_1 > 0,\ B_1 > 0$; (ii) $A_1 > 0,\ B_1 < 0$; and (iii) $A_1 > 0,\ B_1 = 0$. The last of these corresponds to negligible thermal influence, while the first two correspond to negative or positive surface-tension gradient (-γ), in turn. Before describing the nature of the curve obtained in each case, we consider a second example, where this time both reduced buoyancy ($Ra/Pr = 0(r_c^{-4})$ or equivalently $\overline{Ra} = 0$, $\overline{\overline{Ra}} = 0(1)$) and low effective shear on the interface ($AM \ll 1$) are addressed. Then, using (5.5c) together with the temperature sinusoidal approximation, (7.2) yields (again to within $O(r_c^2)$)

$$\hat{R}_2 = A_2 \cos(\pi z) - B_2 \sin(\pi z) \tag{7.4}$$

for $0 < z < 1$, where $A_2 \equiv \bar{\bar{R}}a/2\pi$ and $B_2 \equiv r_c^3 \bar{C} - AM$. The scaled deformation here is $\hat{R}_2 = r_c^3 \hat{R} + D_2/2$, with D_2 denoting the appropriate pressure constant of integration. Again A_2 is positive, while B_2 is positive, negative or zero-valued, according as $r_c^3 \bar{C} > AM$, $r_c^3 \bar{C} < AM$ and $r_c^3 \bar{C} = AM$ respectively. Hence the same three canonical forms identified in the first example are obtained here, although we mention that the different parameter dependences on these conditions show that regimes exist where different deformation types occur. For instance setting $\bar{C}$ to zero (to simulate negligible thermal influence), we can see that case (iii) is relevant when we have significant buoyancy, thereby rendering a pure cosine (antisymmetric) curve for the deformation, while for low buoyancy and low effective shear, the middle case holds, and an interface with a convex 'bulge' develops, possessing a single maximum in the lower half of the domain. Some sample profiles based on the canonical forms are displayed in figure 20, and we note here that the profiles are necessarily incomplete, owing to the breakdown of the core-flow solution near the end-walls. An insightful means of interpreting the canonical forms of (7.3),(7.4) is to employ the alternative '$Q - \phi$' formulation, i.e.

$$\hat{R} = Q \cos(\pi z + \phi), \tag{7.5}$$

where $Q = \sqrt{(A^2 + B^2)}$, $\tan(\phi) = B/A$, and A replaces A_1 in (7.3) and A_2 in (7.4), and so on. With $A > 0$ we can simply regard each of (i)-(iii) (with $A_1 \to A$, $B_1 \to B$) as corresponding respectively to a vertical upward, a vertical downward and a zero phase shift of a cosine curve, antisymmetric in $(0, 1)$ and having amplitude Q. For the first two cases, the shift has magnitude $|\phi|/\pi$ and

hence cannot exceed 1/2; this bound, we note, follows directly from A being positive.

Finally, again in the narrow-domain setting, flow separation may well also occur in at least one of the end regions as the forcing amplitudes increase even though in effect only one of the three boundaries there acts as a solid wall. The present approach combining full simulations and nonlinear limit analysis should extend to allow for this and the other new aspects above.

Acknowledgement

Thanks are due to Dr. H. Kuhlmann for his interest, and to Prof. E. Bänsch for providing the fundamental components of the DNS code.

References

Adler, J. & Sowerby, L. 1970 Shallow three-dimensional flows with variable surface tension. *J. Fluid Mech.* **42**, 549–559.

Babskiy, V. G., Sklovskaya, I. L. & Sklovskiy, Y. B. 1973 In *Space Studies in the Ukraine, no.1: Space Materials Studies and Technology* (ed. G. S. Pisarenko). p. 121. Kiev Naukova Dumka, Kiev.

Bänsch, E. 1998 Simulation of instationary, incompressible flows. *Acta Math. Univ. Comenianae* **LXVII**, 101–114.

Bänsch, E. 2001 Finite element discretization of the Navier–Stokes equations with a free capillary surface. *Numer. Math.* **88**, 203–235.

Bänsch, E. & Höhn, B. 1998 Numerical simulation of a silicon floating zone with a free capillary surface. *Rep.* 98–08. Zentrum für Technomathematik, University of Bremen, Germany.

Birikh, R. V. 1966 *J. Appl. Mech. Tech. Phys.* **7**, 43.

Brezzi, F. & Fortin, M. 1991 *Mixed and Hybrid Finite Element Methods.* Springer–Verlag, New York, New York, U.S.A.

Bristeau, M. O., Glowinski, R. & Periaux, J. 1987 Numerical methods for the Navier–Stokes equations. Applications to the simulation of compressible and incompressible flows. *Computer Physics Report* **6**, 73–188.

Chun, C.–H. & Wuest, W. 1978*a* A microgravity simulation of the Marangoni convection. *Acta Astronautica* **5**, 681–686.

Chun, C.–H. & Wuest, W. 1978*b* *COSPAR: Space Research* **18**, 523.

Chun, C.–H. & Wuest, W. 1979 Experiments on the transition from steady to oscillatory Marangoni convection in a floating zone under reduced gravity effect. *Acta Astronautica* **6**, 1073–1082.

Clark, P. A. & Wilcox, W. R. 1980 Influence of gravity on thermocapillary convection in floating zone melting of silicon. *J. Crystal Growth* **50**, 461–469.

Cuvelier, C. & Driessen, J. M. 1986 Thermocapillary free boundaries in crystal growth. *J. Fluid Mech.* **169**, 1–26.

Davis, S. H. 1987 Thermocapillary instabilities. *Ann. Rev. Fluid Mech.* **19**, 403–435.

DOLD, P., CRÖLL, A. & BENZ, K. W. 1998 Floating-zone growth of silicon in magnetic fields, Part I: weak static axial fields. *J. Crystal Growth* **183**, 545–553.

GIRAULT, V. & RAVIART, P. A. 1986 *Finite Element Methods for Navier–Stokes Equations. Theory and Algorithms.* Springer–Verlag, Berlin, Germany.

KAISER, T. & BENZ, K. W. 1998 Floating-zone growth of silicon in magnetic fields, Part III: numerical simulation. *J. Crystal Growth* **191**, 365–376.

LEVENSTAM, M. & AMBERG, G. 1995 Hydrodynamical instabilities of thermocapillary flow in a half-zone *J. Fluid Mech.* **297**, 357–372.

LEVICH, V. G. 1962 *Physiochemical Hydrodynamics.* Prentice Hall, New York, New York, USA.

LEYPOLDT, J., KUHLMANN, H. C. & RATH, H. J. 2000 Three-dimensional numerical simulation of thermocapillary flows in cylindrical liquid bridges. *J. Fluid Mech.* **414**, 285–314.

MÜLLER, G. & OSTROGORSKY, A. 1994 Convection in melt growth. In *Handbook of Crystal Growth 2B* (ed. D. T. J. Hurle). pp. 709–819. Elsevier Sci., North–Holland, Amsterdam, The Netherlands.

NEPOMNYASHCHY, A. A., SIMANOVSKII, I. B. & BRAVERMAN, L. M. 2001 Stability of thermocapillary flows with inclined temperature gradient. *J. Fluid Mech.* **442**, 141–155.

OSTRACH, S. 1977 In *Physiochemical Hydrodynamics* (ed. D. B. Spalding). Vol. 2, p. 571. Advance, Hudson, WI, USA.

RILEY, R. J. & NEITZEL, G. P. 1998 Instability of thermocapillary-buoyancy convection in shallow layers, Part 1. Characterization of steady and oscillatory instabilities. *J. Fluid Mech.* **359**, 143–164.

RUPP, R., MÜLLER, G. & NEUMANN, G. 1989 Three-dimensional time-dependent modelling of the Marangoni convection in zone melting configurations for GaAs. *J. Crystal Growth* **97**, 34–41.

SAAD, Y. & SCHULTZ, M. H. 1986 GMRES: A generalised minimal residual algorithm for solving nonsymmetric linear equations. *Siam J. Sci. Stat. Comput.* **7(3)**, 856–869.

SCHWABE, D. 1988 Surface-tension-driven flow in crystal growth melts. In *Crystal Growth, Properties and Applications 11.* Springer–Verlag, Berlin, Germany.

SCHWABE, D., SCHARMANN, A., PREISSER, F. & OEDER, R. 1978 Surface tension driven flow in floating zone melting. *J. Crystal Growth* **43**, 305–312.

SEN, A. K. & DAVIS, S. H. 1982 Steady thermocapillary flows in two-dimensional slots. *J. Fluid Mech.* **121**, 163–184.

SMITH, M. K. & DAVIS, S. H. 1983*a* Instabilities of dynamic thermocapillary liquid layers. Part 1. Convective instabilities. *J. Fluid Mech.* **132**, 119–144.

SMITH, M. K. & DAVIS, S. H. 1983*b* Instabilities of dynamic thermocapillary liquid layers. Part 2. Surface-wave instabilities. *J. Fluid Mech.* **132**, 145–162.

TENHAEFF, M. 1997 Berechnung inkompressibler rotationssymmetrischer

Strömungen elektrisch leitender Flüssigkeiten unter dem Einfluss von rotierenden Magnetfeldern. Diploma dissertation, University of Freiburg, Germany.

VELTEN, R., SCHWABE, D. & SCHARMANN, A. 1991 The periodic instability of thermocapillary convection in cylindrical liquid bridges. *Phys. Fluids A* **3**, 267–279.

WANSCHURA, M., KUHLMANN, H. C. & RATH, H. J. 1997 Linear stability of two-dimensional combined buoyant-thermocapillary flow in cylindrical liquid bridges. *Phys. Rev. E* **55**, 7036–7042.

XU, J.–J. & DAVIS, S.H. 1983 Liquid bridges with thermocapillarity. *Phys. Fluids* **26(10)**, 2880–2886.

XU, J.–J. & DAVIS, S.H. 1984 Convective thermocapillary instabilities in liquid bridges. *Phys. Fluids* **27**, 1102–1107.

XU, J.–J. & DAVIS, S.H. 1985 Instability of capillary jets with thermocapillarity. *J. Fluid Mech.* **161**, 1–25.

YIH, C.–S. 1968 *Phys. Fluids* **11**, 477.

YIH, C.–S. 1969 Three-dimensional motion of a liquid film induced by surface-tension variation or gravity. *Phys. Fluids* **12**, 1982–1987.

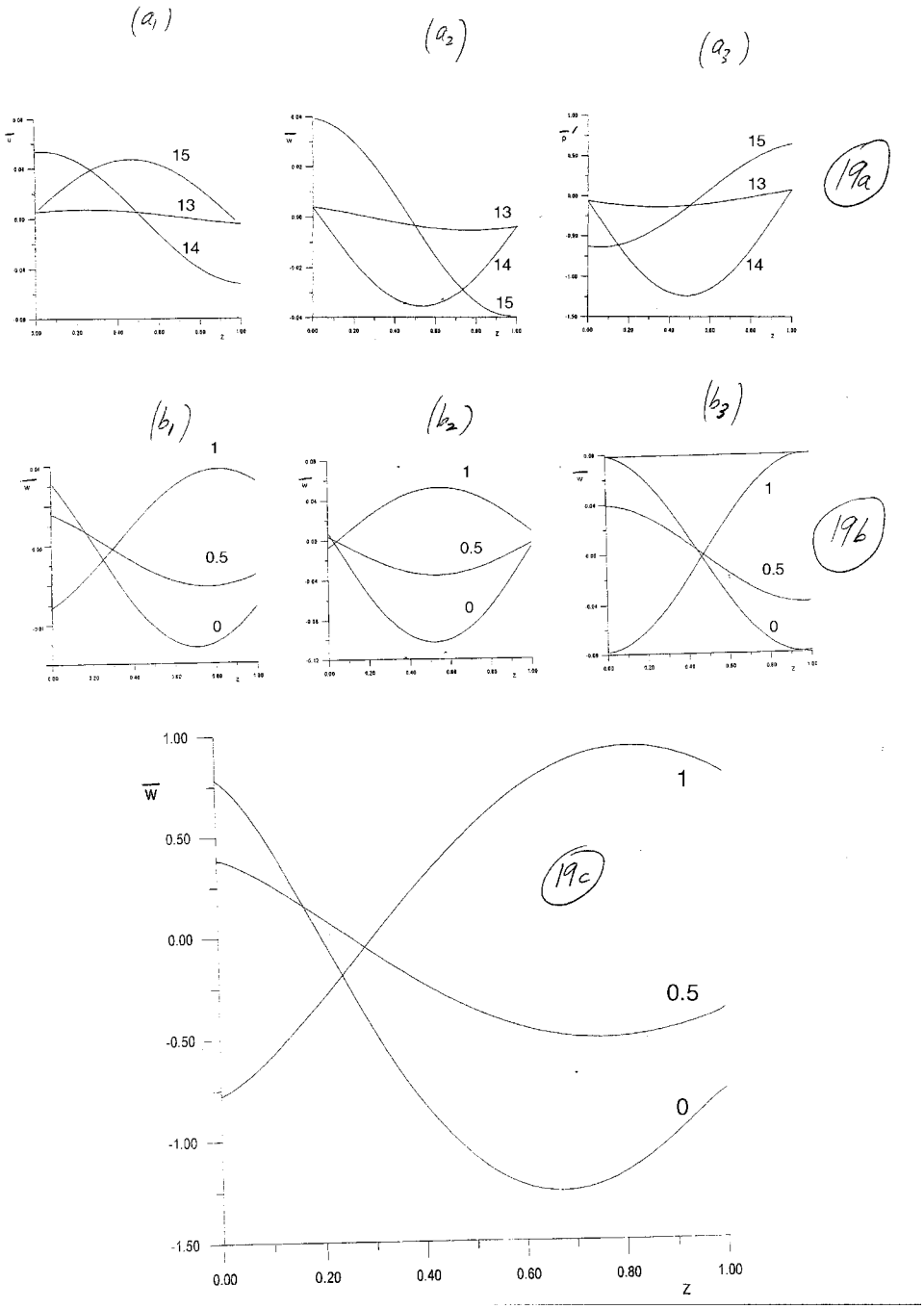

Figure 19: Buoyancy effects in slender flow. (a) $\bar{u}, \bar{w}$ at $\bar{r} = \frac{1}{2}$, and $\bar{p}'$, vs. z, for cases $(AM, \overline{Ra}) = (0.01, 0.1), (0.01, 1), (0.1, 0.1)$ labelled $13, 14, 15$ in turn. (b) For the three cases, in turn, showing $\bar{w}$ at $\bar{r} = 0, \frac{1}{2}, 1$, vs. z. (c) Scaled profiles $\bar{w}$ vs. z at $\bar{r} = 0, \frac{1}{2}, 1$ in the case $(AM, \overline{Ra}) = (1, 10)$.

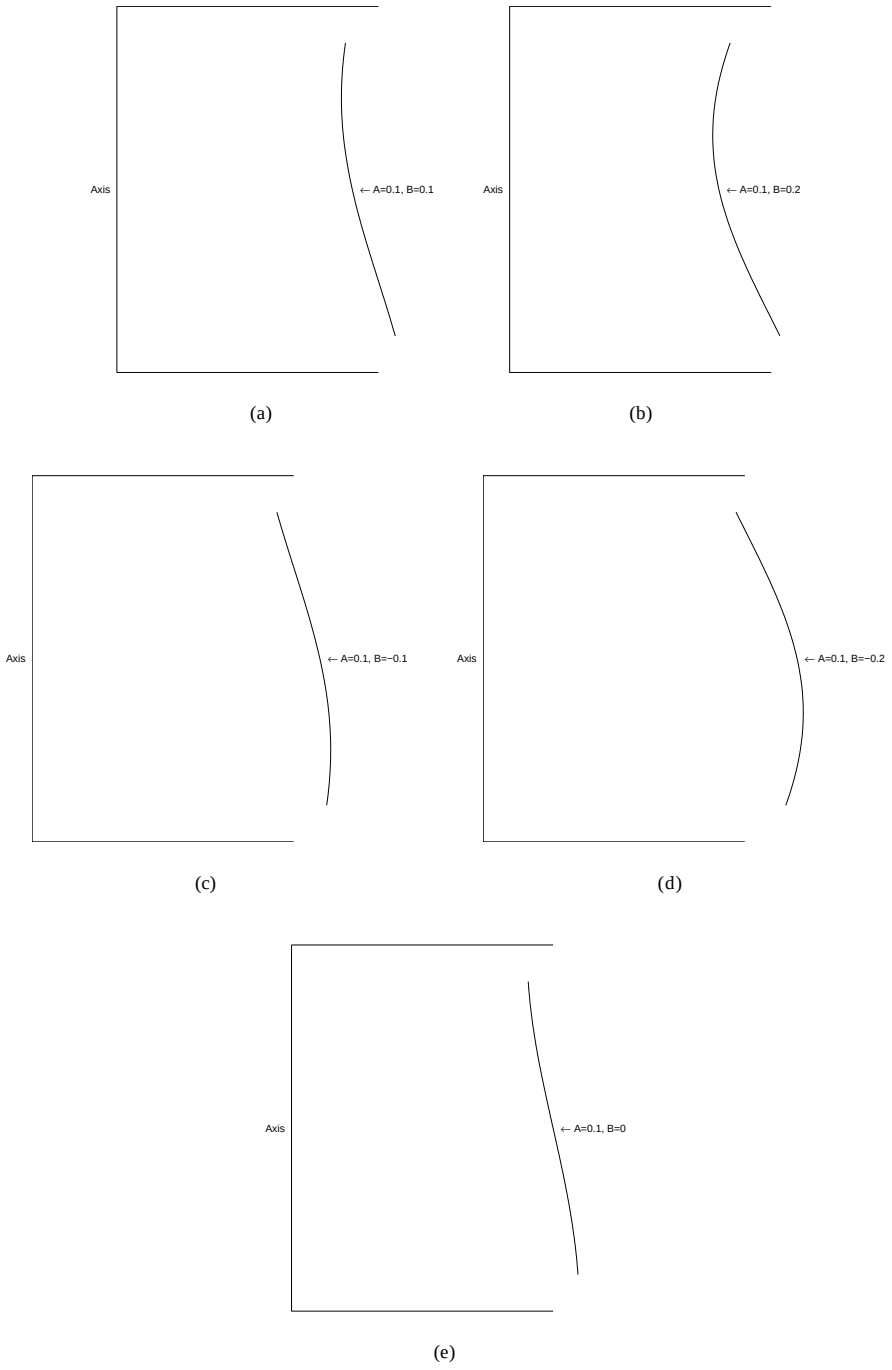

Figure 20: Liquid-gas interface profiles for small deformations (scaled up for clarity) based on computing (7.5) for $A = 0.1$ with B equal to (a) 0.1; (b) 0.2; (c) -0.1; (d) $-0.2, (e)$ 0.